7 Analysis of Neural Excitability and Oscillations

John Rinzel and Bard Ermentrout

7.1 Introduction

Qualitative features of excitable or oscillatory dynamics are shared by broad classes of neuronal models. Expressed in models for single-cell behavior as well as for ensemble activity, these features include excitability and threshold behavior; beating and bursting oscillations and phase locking; and bistability and hystersis. Our goal here is to illustrate, by exploiting a specific model of excitable membrane, some of the concepts and techniques that can be used to understand, predict, and interpret these dynamic phenomena biophysically. Our mathematical methods include numerical integration of the model equations, graphical or geometric representation of the dynamics (phase plane analysis), and analytic formulae for characterizing thresholds and stability conditions. The concepts are from the qualitative theory of nonlinear differential equations and nonlinear oscillations, and from perturbation and bifurcation theory. In this brief chapter, we will not consider the spatiotemporal aspects of distributed systems. Thus our methods apply directly only to a membrane patch, to a spatially uniform, equipotential cell, or to a network with each cell type perfectly synchronized.

Even seemingly simple models that exhibit one or two of the different dynamic behaviors, such as generation of individual or repetitive action potentials, may display a great variety of response characteristics when a broad range of parameters is considered. This means that a given cell or ensemble may behave in many different modes, for example, as a generator of single pulses, as a bursting pacemaker, as a bistable "plateauing" cell, or as a beating oscillator, depending upon the physiological conditions (neuromodulator or ionic concentrations) or stimulus presentations (applied currents or synaptic inputs). The nonlinear nature of the models provides the substrate for this broad repertoire; in contrast, linear models may be characterized by exponential or oscillatory time courses over their entire parameter ranges. It is important when studying a nonlinear model that stimulus-response properties be considered over ranges of the biophsical parameters.

In this chapter, we show that a simple, but biophysically reasonable, two-current excitable membrane model is sufficiently robust to exhibit such behavioral richness, as parameters are systematically varied. By adjusting channel densities, activation dynamics, and stimulus intensities, we find that the cell model can exhibit quite different threshold characteristics for spike generation (finite or infinite latency, with or without intermediate amplitude responses) and for onset of repetitive firing (finite or zero minimum frequency). The cell shows various types of bistable behavior: two

different rest states, in one case, and a rest state with a coexistent oscillatory response around a depolarized level, in another. The latter situation can provide a mechanism for rhythmic bursting when additional slower processes (e.g., slow channel kinetics, or a channel affected by slow ion accumulation) respond differently at the two potential levels. Because the spike-generating dynamics significantly influence the burst's waveform, there can be several different types of bursting depending on the nature of the fast dynamics; for example, parabolic bursting does not depend on bistability in the spike-generating processes. Finally, by considering the phase-resetting behavior for a self-oscillatory cell, we show that the response to a single brief, arbitrarily timed, perturbing stimulus can often be used to predict phase-locking responses to periodic stimulation, and to predict the synchronization properties of weakly coupled cells.

The underlying qualitative structure for these behaviors will be revealed with graphical phase plane analysis, complemented by a few analytic formulas. The concepts we will cover include steady states, trajectories, limit cycles, stability, domains of attraction, and bifurcation of solutions. Phase plane characteristics and system dynamics will be interpreted biophysically in terms of activation curves, current-voltage relations, and the like. A user-friendly program, XPP (developed by G. B. Ermentrout) for X-windows computers allows modelers to interactively generate, explore, and visualize most of the behaviors described here in the same spirit as an experimental "setup." (XPP's numerical procedures are summarized in chapter appendix B.) The concepts apply to higher-order systems, for which appropriate projections of phase space, motivated by differences in time scales for certain variables, can lead to similar insights.

7.2 Models for Excitable Cells and Networks

Most models for excitable membrane retain the general Hodgkin-Huxley (HH) format (Hodgkin and Huxley 1952), and can be written in the form

$$C\frac{dV}{dt} + I_{ion}(V, W_1, \ldots, W_n) = I(t) \tag{7.1}$$

$$\frac{dW_i}{dt} = \phi\frac{[W_{i,\infty}(V) - W_i]}{\tau_i(V)}, \tag{7.2}$$

where V denotes membrane potential (say, deviation from a reference, or "rest" level), C is membrane capacity, and I_{ion} is the sum of V- and t-dependent currents through the various ionic channel types; $I(t)$ is the applied current. The $W_i(t)$ vari-

ables describe the fraction of channels of a given type that are in various conducting states (e.g., open or closed) at time t. The first-order kinetics for W_i typically involve V dependence in the time constant τ_i; ϕ is a temperature-like time scale factor that may depend on i. If the current, I_j, for channel type j may be suitably modeled as ohmic, then it might be expressed as

$$I_j = \bar{g}_j \sigma_j(V, W_1, \ldots, W_n)(V - V_j), \tag{7.3}$$

where $\bar{g}_j$ is the total conductance with all j-type channels open (product of single-channel conductance with the total number of j channels), σ_j is the fraction of j channels that are open (it may depend on several of the W_i variables), and V_j is the reversal potential (usually Nernstian) for this ion species. For some channel types the current-voltage relation may be more appropriately represented by the Goldman-Hodgkin-Katz equation, or by a barrier kinetics scheme (Hille 1992), and the gating kinetics might involve a multistate Markov description. In the classical HH model (Hodgkin and Huxley 1952) for squid giant axon, there are three variables W_i, denoted as m, h, and n, to describe the fractions m^3h and n^4 of open Na^+ channels and K^+ channels, respectively.

For some purposes, it is important that the current balance equation (eq. 7.1) contain terms to account for ionic pump currents. These currents, as well as some channel conductances, may depend upon time-varying second messengers or ionic concentrations, for example, in diffusionally restricted intracellular or extracellular volumes. For such considerations, additional variables and transport or kinetic balance equations would be included in the model, and these will carry along their own time scales. Indeed, some models that include the dynamics of intracellular free calcium handling have assumed time constants that are orders of magnitude greater than channel kinetics and thereby set the time scale for phenomena such as bursting oscillations (see, for example, Chay and Keizer 1983). We also note that the form of eq. 7.2 is not unique; in a phenomenological model of Rall (see Goldstein and Rall 1974), the corresponding equations are nonlinear in the W_i.

Some models for excitability contain many variables and represent numerous channel types, especially models designed to account for rather detailed aspects of spike shape and dependence on many different pharmacological agents. On the other hand, if qualitative or semiquantitative characteristics of spike generation and input-output relations are adepuate, say in network simulations, then a reduced model having just a few variables may suffice. Such reductions can sometimes be obtained when time scale differences allow relatively fast variables to be instantaneously relaxed to pseudo–steady-state values; thus, if τ_j is small relative to other time constants, then one might set $W_j = W_{j,\infty}(V)$ in eq. 7.2. Likewise, functionally related

variables with similar time scales might be lumped together. In this spirit, FitzHugh (1960) considered reductions of the HH model (see also Rinzel 1985; Kepler, Abbott, and Marder 1992) and then introduced (FitzHugh 1961) and idealized, analytically tractable two-variable model (see also Nagumo, Arimoto, and Yoshizawa 1962) widely studied as a qualitative prototype for excitable systems in many biological and chemical contexts. A FitzHugh-Nagumo/Hodgkin-Huxley hybrid was formulated and studied by Morris and Lecar (1981), in the context of electrical activity of the barnacle muscle fiber. The model incorporates a V-gated Ca^{2+} channel and a V-gated, delayed-rectifier K^+ channel; neither current inactivates. A simple version of this model is represented by the equations

$$C\frac{dV}{dt} = -I_{ion}(V,w) + I \tag{7.4}$$

$$\frac{dw}{dt} = \phi\frac{[w_\infty(V) - w]}{\tau_w(V)}, \tag{7.5}$$

where

$$I_{ion}(V,w) = \bar{g}_{Ca}m_\infty(V)(V - V_{Ca}) + \bar{g}_K w(V - V_K) + \bar{g}_L(V - V_L). \tag{7.6}$$

In eqs. 7.4–7.6, w is the fraction of K^+ channels open, and the Ca^{2+} channels respond to V so rapidly that we assume instantaneous activation. One might introduce dimensionless variables, as in FitzHugh 1969 or Rinzel and Ermentrout 1989, in order (1) to reduce the number of free parameters and identify equivalent groups of parameters, and (2) identify and group "fast" and "slow" processes together. However, in the interest of clarity, we will keep all equations in their original form. In eq. 7.5, τ_w has been scaled so its maximum is now one, and ϕ equals the temperature factor divided by the prescaled maximum ($1/\sqrt{\lambda_w}$ in Morris and Lecar 1981). (The V-dependent functions, m_∞, w_∞, and τ_w, and the reference parameter sets are given in appendix A). All the computations and figures in this chapter are based on eqs. 7.4–7.6, and extensions of them for generating bursting behaviors.

Even network models in certain approximations can reduce to a few variables. One example is the Wilson-Cowan model (1972; for another, see chapter 11, this volume):

$$\mu_e\frac{d\mathscr{E}}{dt} = -\mathscr{E} + S(\alpha_{ee}\mathscr{E} - \alpha_{ie}\mathscr{I} - \theta_e) \tag{7.7}$$

$$\mu_i\frac{d\mathscr{I}}{dt} = -\mathscr{I} + S(\alpha_{ei}\mathscr{E} - \alpha_{ii}\mathscr{I} - \theta_i), \tag{7.8}$$

where $\mathscr{E}$ and $\mathscr{I}$ represent the respective firing rates of a population of excitatory and inhibitory interneurons. The parameters μ_e, μ_i are the membrane time constants; θ_e, θ_i are the firing thresholds; α_{ee}, α_{ie}, α_{ei}, α_{ii} are the "synaptic weights"; and $S(\cdot)$ is a nonlinear saturating function similar in form to $m_\infty(V)$.

7.3 Understanding Dynamics via Phase Plane Analysis

While an experimenter typically can measure membrane potential, it is usually impossible to monitor other dynamic variables, such as ionic currents, during nonclamped activity. For a theoretical model, we must explicitly compute the time courses of all dependent variables; we can then compare the time courses of the different dynamic variables and identify their contributions and temporal relationships. A valuable way to view the response of multiple variables and their relationship to physiological functions at the same time is by phase plane profiles, that is, curves of one dependent variable against another. Moreover, such plots allow us also to geometrically represent and interpret aspects of the model (e.g., activation curves) along with the response trajectories. At a glance, we can see whether the model has one or multiple steady states, which stimuli might invoke switching between states, and where these steady states lie in relation to activation and current-voltage (I-V) characteristics. While the phase plane view provides a full description for two-variable models, judicious two-dimensional projections from phase spaces of higher-order systems can yield some of these same insights.

Phase plane analysis was used effectively by FitzHugh (1960, 1961, 1969) to understand various aspects of the HH equations and the two-variable FitzHugh-Nagumo model. (FitzHugh 1969 also defines some basic mathematical terminology of nonlinear dynamics and supplements our presentation; for additional mathematical introduction, see also Edelstein-Keshet 1988 and Strogatz 1994.)

7.3.1 The Geometry of Excitability

We begin by considering the Morris-Lecar model (1981), in the case that there is a unique rest state and a thresholdlike behavior for action potential generation. Figure 7.1A shows the V responses to brief current pulses of different amplitudes. The peak V is graded, but the variation occurs over a very narrow range of stimuli; in this case, as in the standard HH model, the threshold phenomenon is not discrete, but rather, steeply graded. In figure 7.1B, these same responses are represented in the V-w plane. The solution path in the space of dependent variables is called a "trajectory," and direction of motion along a trajectory is often indicated by an

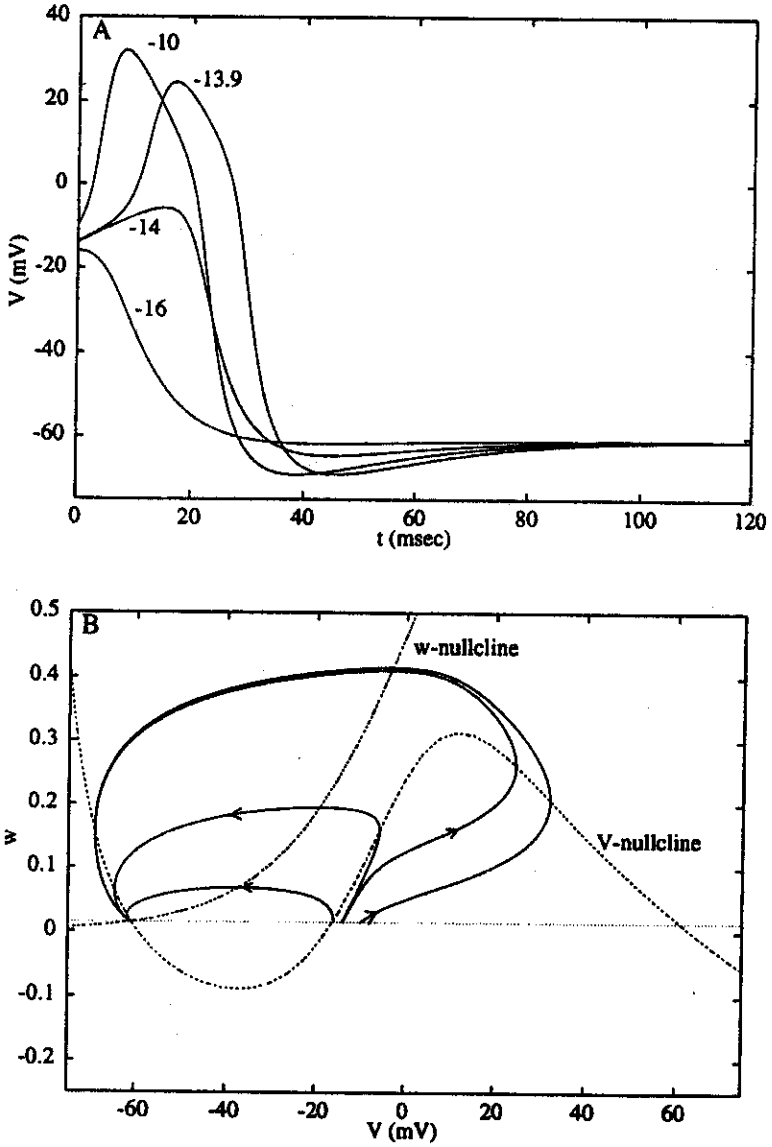

Figure 7.1
Response of the Morris-Lecar excitable system, eqs. 7.4–7.6, to a brief current pulse. For these parameters (see appendix A), the system has a unique stable rest state, $\bar{V} = -61\,\text{mV}$, $\bar{w} = .015$. The line $w = \bar{w}$ is shown lightly dashed. Four different stimuli lead to an instantaneous displacement of V from $\bar{V}$ to V_0 (values of V_0 are shown alongside the curves in panel A). Panel A shows the time course of the voltage. Notice that intermediate responses are possible with some stimuli: the threshold is graded; firing occurs with finite latency. Panel B shows trajectories in the V-w phase plane; nullclines are shown dashed and intersect only once. The effect of a stimulus is to displace the initial condition horizontally from rest.

arrowhead. In figure 7.1B, the flow is generally counterclockwise. All the trajectories shown here ultimately lead to the rest point: $V = \bar{V}, w = \bar{w} = w_\infty(\bar{V})$. The rest state is said to be "globally attracting." Each trajectory has a unique initial point, a horizontal displacement from the rest point corresponding to instantaneous depolarization by a brief current pulse. A trajectory's slope conveys the relative speed of w to V; thus a shallow slope means V is changing faster (see next paragraph). The trajectory of an action potential shows the following features: an upstroke with rapid increase in V (trajectory is moving rightward with little vertical component) and then the transient depolarized plateau with the delayed major increase in w, corresponding to the slower opening of K^+ channels. When w is large enough, the abrupt downstroke in V occurs—the trajectory moves leftward, nearly horizontal, as V tends toward V_K. Finally, as w decreases (the potassium channels close), the state point returns to rest with a slow recovery from hyperpolarization.

In the phase plane, the slope of a trajectory at a given point is dw/dV, which is simply the ratio of dw/dt to dV/dt, and these quantities are evaluated from the right-hand sides of the differential equations (eqs. 7.4–7.5). (The program XPP has a command to plot short vectors that indicate the flow pattern generated by the equations. This allows a global view of the flow without having to compute the trajectories. The program also computes nullclines, defined next.) Thus a trajectory must be vertical or horizontal where $dV/dt = 0$ or $dw/dt = 0$, respectively. The conditions

$$0 = -\bar{g}_{Ca} m_\infty(V)(V - V_{Ca}) - \bar{g}_K w(V - V_K) - \bar{g}_L(V - V_L) + I \tag{7.9}$$

$$0 = \phi \frac{[w_\infty(V) - w]}{\tau_w(V)} \tag{7.10}$$

define curves, the V and w nullclines, which are shown dashed in figure 7.1B. This provides a geometrical realization for where V and w can reach their maximum and minimum values along a trajectory in the V-w plane (notice how the trajectories cross the nullclines either vertically or horizontally in figure 7.1B). The w nullcline is simply the w activation curve, $w = w_\infty(V)$. The V nullcline, from eq. 7.9, corresponds to V and w values at which the instantaneous ionic current plus applied current is zero; below the V nullcline, V is increasing and above it, V is decreasing. The cubic-like shape seen here reflects the N-shaped *instantaneous I-V relation*, $I_{ion}(V, w)$ versus V with w fixed (eq. 7.6), typical of excitable membrane models in which the V-gated channels carrying inward current activate rapidly. From another viewpoint, motivated by the slower time scale of w, suppose we fix w, say, at a moderate value. Then the three points on the V nullcline at this w correspond to three pseudo–steady

states; at the low-V state, small outward and inward currents cancel while at the high-V state, both currents are larger but are again in balance. These states are transiently visited during the plateau phase and the return-to-rest phase of an action potential. Notice how the trajectory is near the right and left branches of the V nullcline during these phases.

If ϕ were smaller still, then the phase plane trajectories (except when near the V nullcline) would be nearly horizontal (because dw/dV would be small); the action potential trajectory during the plateau and recovery phases would essentially cling to, and move slowly along, either the right or left branch of the V nullcline. The downstroke would occur at the knee of the V nullcline. The time course would be more like that of a cardiac action potential. Also, in the case of smaller ϕ, the threshold phenomenon would be extremely steep; the middle branch of the V nullcline would act as an approximate separatrix between sub- and superthreshold initial conditions. In contrast, for larger ϕ, the response amplitude is more graded. This theoretical conclusion led Cole, Guttman, and Bezanilla (1970) to demonstrate experimentally that, at higher temperatures, the action potential for squid axon does not behave in an all-or-none manner.

We note that phase plane methodology applies to autonomous systems, whose equations have no explicit time dependence and whose nullclines and flow field therefore do not change with time. (This would not be the case if, for example, I were periodic in t; periodic stimuli will be covered later.) The phase plane method extends, however, to cases where a step change in a parameter occurs. At the time a parameter's value jumps, the nullclines would change instantaneously, but not the present location of V and w. FitzHugh (1961) uses this trick to interpret anodal break excitation, and Somers and Kopell (1993) have used this to analyze the behavior of coupled Morris-Lecar oscillators when ϕ is very small.

7.3.2 Oscillations Emerging with Nonzero Frequency

In the phase plane treatment, the rest state of the model is realized as the intersection of the two nullclines; such steady-state solutions are also referred to as singular or equilbrium points. From the geometrical viewpoint, one sees how different parameter values could easily lead to multiple singular points—by changing the shapes and positions of the nullclines. In figure 7.1, the unique singular point is attracting. Technically, we say it is asymptotically stable, that is, for any nearby initial point the solution tends to the singular point as $t \to \infty$. In general, the local stability of a singular point can be determined by a simple algebraic criterion (Edelstein-Keshet 1988; Strogatz 1994). The procedure is to linearize the differential equations, evaluate the partial derivatives at the singular point (this matrix of partial derivatives is

called the Jacobian), and to determine whether the exponential solutions to this constant coefficient system have any growing modes. If so, then the singular point is unstable; if all modes decay, then it is stable. For eqs. 7.4–7.6, the linearized equations that describe the behavior of small disturbances, $V \approx \bar{V} + x$, $w \approx \bar{w} + y$, from the singular point are

$$\frac{dx}{dt} = ax + by \tag{7.11}$$

$$\frac{dy}{dt} = cx + dy, \tag{7.12}$$

where

$$a = -\frac{\partial I_{ion}(V, w)}{\partial V} \tag{7.13}$$

$$b = -\frac{\partial I_{ion}(V, w)}{\partial w} \tag{7.14}$$

$$c = \frac{\phi}{\tau_w} \frac{dw_\infty}{dV} \tag{7.15}$$

$$d = -\frac{\phi}{\tau_w}. \tag{7.16}$$

Solutions are of the form $\exp(\lambda_1 t)$, $\exp(\lambda_2 t)$, where $\lambda_{1,2}$ are the eigenvalues of the Jacobian matrix in eqs. 7.11–7.12; they are roots of the quadratic

$$\lambda^2 - (a + d)\lambda + (ad - bc) = 0. \tag{7.17}$$

For the parameters of figure 7.1, the two eigenvalues are both real and negative.

As parameters are varied, the singular point may lose stability. In our example, the rest state could then no longer be maintained and the behavior of the system would change—it may fire repetitively or tend to a different steady state (if a stable one exists). Let us consider the effect of a steady applied current and ask how repetitive firing arises in this model. We will apply linear stability theory to find values of I for which the steady state is unstable. First, we note that for eqs. 7.4–7.6, and for nerve membrane models of the general form of eqs. 7.1–7.2, a steady-state solution $\bar{V}$ for a given I must satisfy $I = I_{ss}(\bar{V})$, where $I_{ss}(V)$ is the steady-state I-V relation of the model given by

$$I_{ss}(V) = I_{ion}(V, w_\infty(V)). \tag{7.18}$$

If I_{ss} is N-shaped, there will be three steady states for some range of I. If however, I_{ss} is monotonic increasing with V, as in the case of figure 7.1, then there is a unique $\bar{V}$ for each I; moreover, $(\bar{V}, \bar{w})$ cannot lose stability by having a single real eigenvalue pass through zero. Destabilization can only occur by a complex conjugate pair of eigenvalues crossing the axis $Re\,\lambda = 0$ as I is varied through a critical value I_1. At such a transition, a periodic solution to eqs. 7.4–7.6 is born—and we have the onset of repetitive activity. This solution, for I close to I_1, is of small amplitude and frequency proportional to $Im\lambda$. Emergence of a periodic solution in this way is called a Hopf bifurcation (Edelstein-Keshet 1988; Strogatz 1994).

From eqs. 7.11–7.12, or eq. 7.17, we know that $\lambda_1 + \lambda_2 = a + d$. Thus loss of stability occurs for the I whose corresponding $\bar{V}$ satisfies

$$\frac{\partial I_{ion}(V, w)}{\partial v} + \frac{\phi}{\tau_w} = 0. \tag{7.19}$$

The first term here is the slope of the instantaneous I-V relation and the second is the rate of the recovery process; this condition also applies approximately to the HH model (Rinzel 1978). From eq. 7.19 we conclude that loss of stability occurs: (1) only if the *instantaneous I-V relation* has negative slope at $\bar{V}$; (2) when the destabilizing growth rate of V from this negative resistance just balances the recovery rate; and (3) only if recovery is sufficiently slow, i.e. if ϕ is small (low "temperature"). In figure 7.2A, $\bar{V}$ is plotted versus I (this is the *steady-state I-V relation*, but shown as V against I) and the region of instability is shown dashed.

Figure 7.2A also shows the maximum and minimum values of V for the oscillatory response. Just as a singular point can be unstable, so, too, can a periodic solution (Strogatz 1994); unstable periodics are indicated by open circles. Here we see that the small amplitude periodic solution born at $I = I_1 = 93.85\,\mu A/cm^2$ from the loss in stability of $\bar{V}$ is itself unstable; it would not be directly observable. (In the phase plane, but not generally for higher-order systems, an unstable periodic orbit can be determined by integrating backward in time.) Note that solutions along this branch depend continuously on parameters and they gain stability at the turning point or knee at $I = I_v = 88.3\,\mu A/cm^2$. A stable periodic solution is called a "limit cycle." The upper branch (solid) corresponds to the limit cycle of observed repetitive firing. The frequency increases with I over most of this branch (figure 7.2B). At sufficiently large I, repetitive firing ceases (depolarization block) as $\bar{V}$ regains stability at $I = I_2 = 212\,\mu A/cm^2$. This figure is referred to as a "bifurcation diagram"; it depicts steady-state and periodic solutions, and their stability, as functions of a parameter

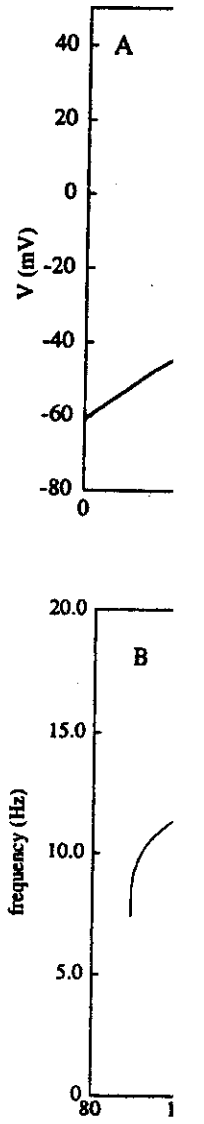

Figure 7.2
Repetitive firing ir
steady-state voltag
minimum voltage
branch of periodi
$I = I_2 = 212\,\mu A/c$
with the stable bra
$215\,\mu A/cm^2$. For t
that the frequency
bounded away fro

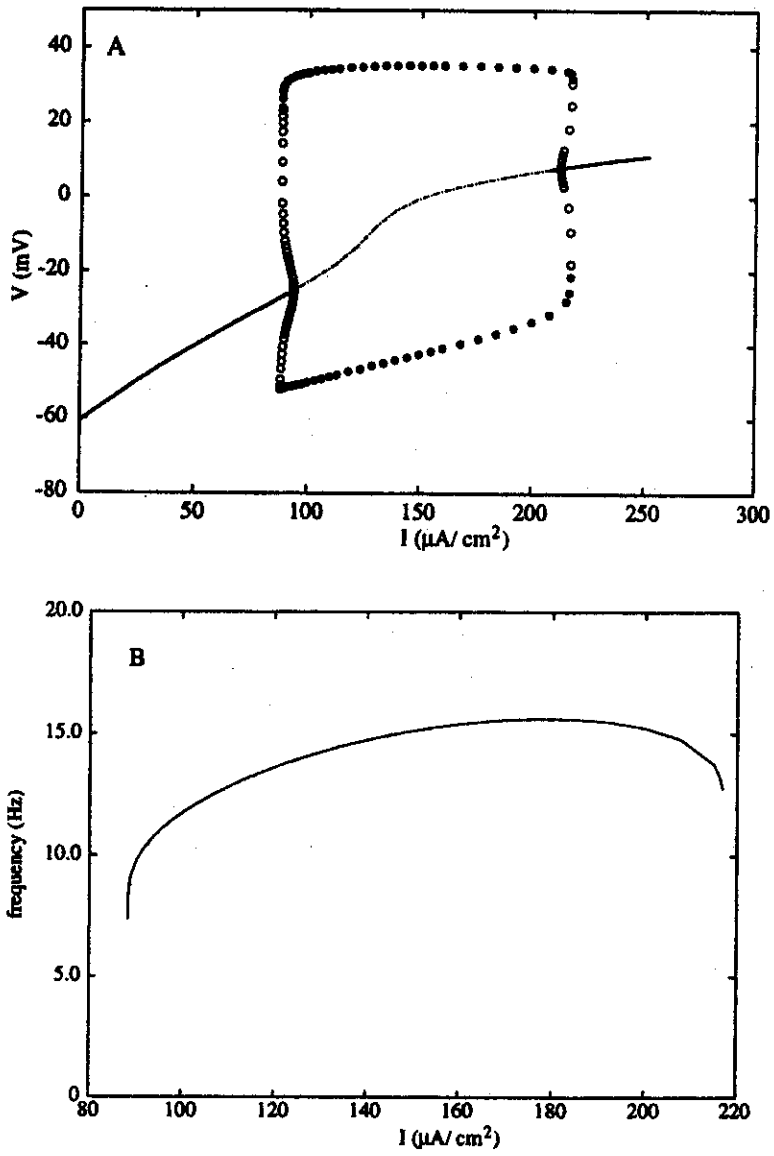

Figure 7.2
Repetitive firing in the Morris-Lecar model for steady current. Bifurcation diagram in panel A shows the steady-state voltage $\bar{V}$ versus I (thin lines; stable are solid, unstable are dashed) and the maximum and minimum voltage for periodic solutions shown as filled (stable) and unfilled (unstable) circles. The unstable branch of periodic solutions meets the branch of steady-state oscillations at $I = I_1 = 94\,\mu A/cm^2$ and $I = I_2 = 212\,\mu A/cm^2$ (Hopf bifurcation points). The unstable branch of periodic solutions coalesces with the stable branch of periodic solutions at $I = I_v = 88\,\mu A/cm^2$. A similar coalescence occurs near $I = 215\,\mu A/cm^2$. For these parameters, the steady-state I-V curve is monotonic. Furthermore, panel B shows that the frequency (plotted in Hz, and only for the stable limit cycles) as a function of current is always bounded away from zero. Parameters are as figure 7.1.

and it shows where one branch *bifurcates* (from the Greek word for branch) from another. Bifurcation theory allows one to characterize solution behavior analytically in the neighborhood of bifurcation points; for example, the frequency of the emergent oscillation at the Hopf point is proportional to $|Im\lambda_{1,2}|$. When the Hopf bifurcation leads to unstable periodic solutions, i.e., when the emergent branch bends back into the parameter region where the steady state is stable, then the bifurcation is *subcritical* (i.e., a hard oscillation); if the opposite occurs, it is *supercritical.*

For a range of I values (between the knee, I_v and the Hopf bifurcation, I_1), our model exhibits *bistability*: a stable steady state and a stable oscillation coexist. Figure 7.3A illustrates the phase plane profile in such a case; a periodic response here appears as a closed orbit. There is a stable fixed point shown as the intersection of the two nullclines and a stable periodic orbit (labeled SPO). The two attractors are separated by an unstable periodic orbit (UPO). Initial values inside the unstable orbit tend to the attracting steady state, while initial conditions outside of it will lead to the limit cycle of repetitive firing. A brief current pulse, whose phase and amplitude are in an appropriate range, can switch the system out of the oscillatory response back to the rest state. Such behavior has been seen for many models and observed, for example, in squid axon membrane (Guttman, Lewis, and Rinzel 1980). In figure 7.3B, two 30 $\mu A/cm^2$ current pulses 5 msec in duration are given, at $t = 100$ msec and then at $t = 470$ msec. The first pulse switches the membrane from rest to repetitive firing, while the second pushes the membrane back to rest. This bistable behavior is critical for the occurence of bursting oscillations when a very slow conductance is added to the model.

7.3.3 Oscillations Emerging with Zero Frequency

The Hopf bifurcation is one of a few generic mechanisms for the onset of oscillations in nonlinear differential equation models. In that case, the frequency at onset of repetitive activity has a well-defined, nonzero minimum. In contrast, some membranes and models (see, for example, Connor, Walter, and McKown 1977) exhibit zero (i.e., arbitrarily low) frequency as they enter the oscillatory regime of behavior; Rall's model (Goldstein and Rall 1974) also behaves this way. A basic feature in such systems is that I_{ss} versus V is N-shaped rather than monotonic, as in the previous section. For eqs. 7.4–7.6, this occurs if the V dependence of K^+ activation is translated rightward (see appendix A, and note value of V_3), so that the inward component of I_{ss} dominates over an intermediate V range. Thus, for some values of I, below the repetitive firing range, there are three singular points in the phase plane and the system is excitable. We discuss this case first. In figure 7.4B, we see the nullclines

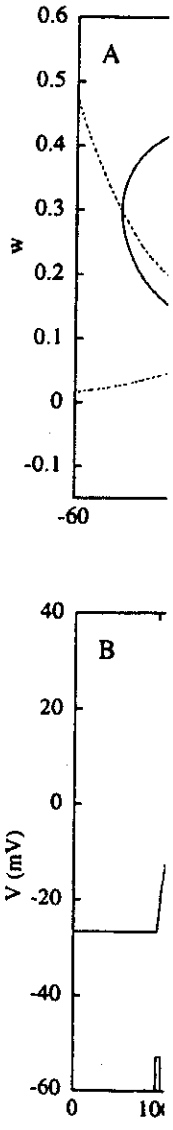

Figure 7.3
Bistability for ste
parameters as in
tion point, I_1, anc
the nullclines) an
shown in panel A
brief appropriatel

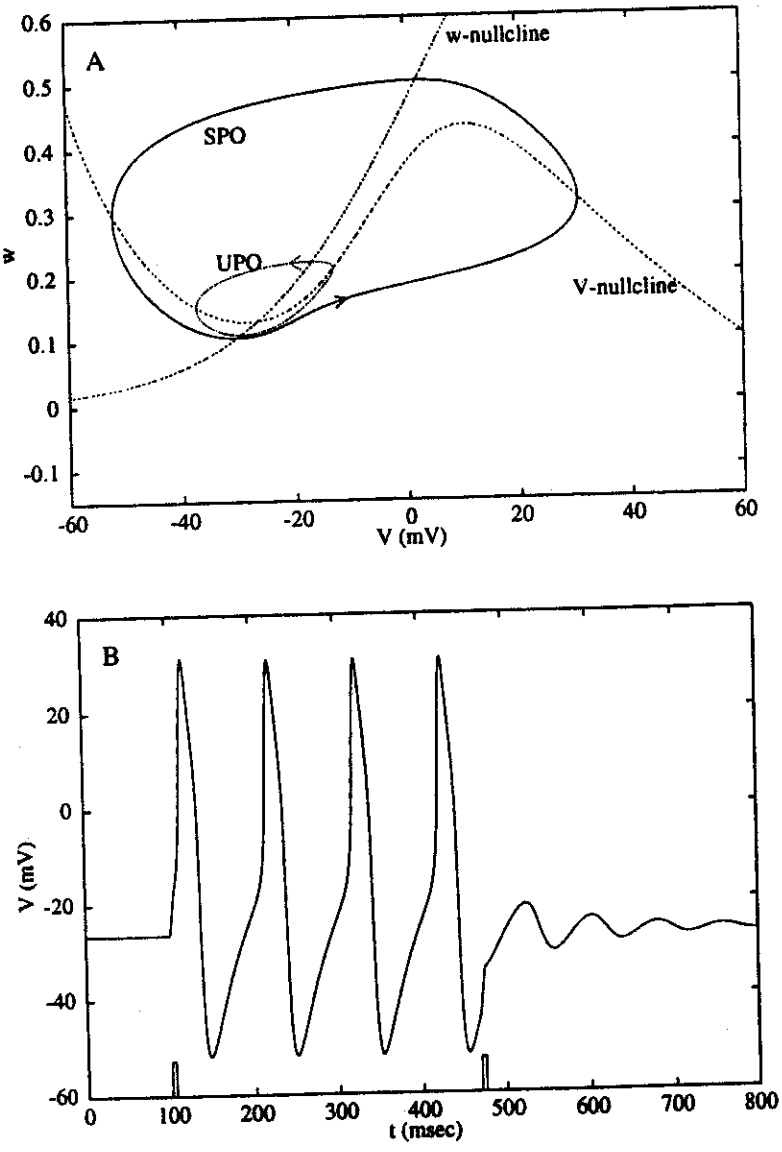

Figure 7.3
Bistability for steady current near the threshold for repetitive firing for the Morris-Lecar model with parameters as in figure 7.1 and $I = 90\,\mu A/cm^2$. In this region, where I is between the first Hopf bifurcation point, I_1, and the "knee," I_ν, there are two stable states (cf figure 7.2): a rest state (the intersection of the nullclines) and a stable oscillation (SPO) separated by an unstable periodic solution (UPO). This is shown in panel A. Panel B demonstrate switching from rest to oscillation and then back to rest for two brief appropriately timed depolarizing current pulses.

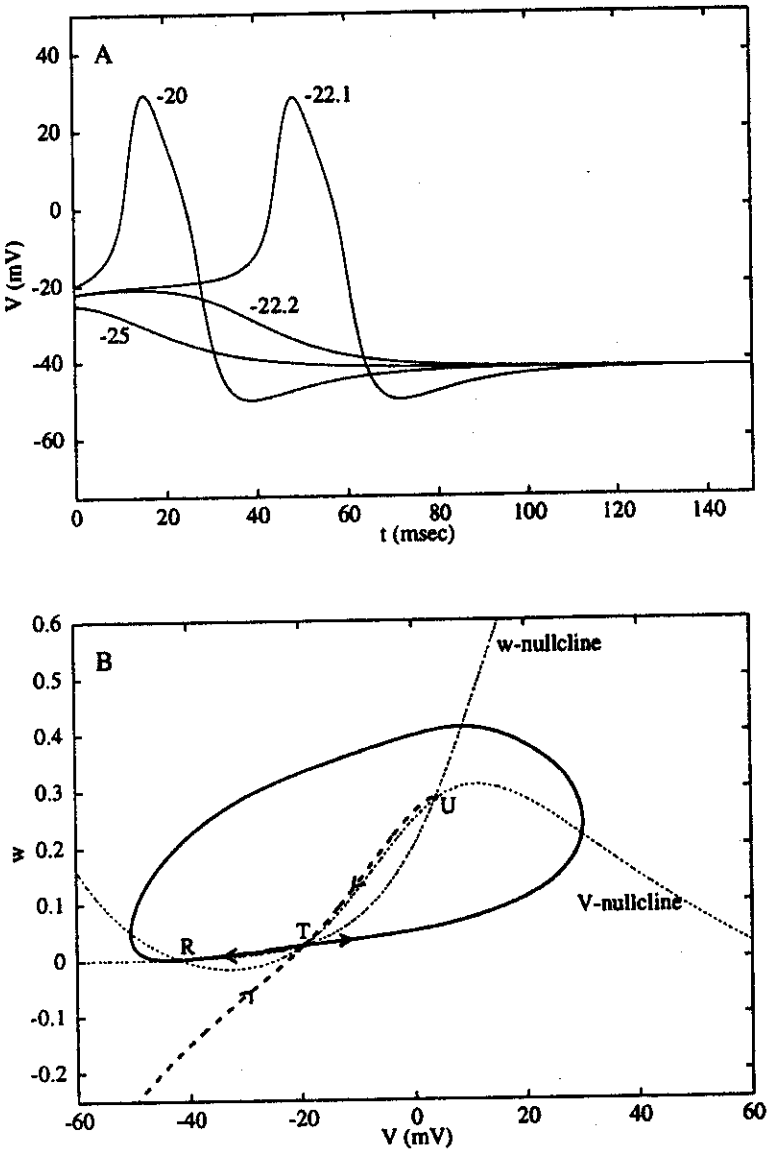

Figure 7.4
Excitability with three steady states and a distinct threshold; the response of the membrane to a brief current pulse from the stable rest state. Four different stimuli result in a displacement of V from $\bar{V}$ to V_0 (values of V_0 are given alongside the curves in panel A). (A) Time course of the voltage for $I = 30\,\mu A/cm^2$. (B) Phase plane for the dynamics illustrated in panel A. Nullclines intersect at three places: (1) R a stable rest state, (2) T, a saddle point threshold, and (3) U an unstable node. The thick solid line shows the unstable manifold for the saddle point; here, unstable refers to movement in opposing directions away from T (indicated by arrowheads). The manifold's two branches lead to the stable rest state and form a smooth loop in phase space. The heavy dashed line shows the stable manifold for the saddle point (arrowheads pointing toward T). Any initial conditions to the left of this manifold decay to rest. Initial conditions to the right lead to an action potential before returning to rest. Parameters are as in figure 7.1, except $\bar{g}_{Ca} = 4\,mS/cm^2$, $V_3 = 12\,mV$, $V_4 = 17.4\,mV$, $\phi = 1/15$.

intersecting thr
are the stable
stable spiral (U
attracting rest
larger stimuli l
The phase plan
distinct thresho
this, we note th
ries (bold dash
matrix; togethe
eigenvalue are
these are the u
folds.) The stab
distinguishes su
the threshold s
threshold respo
not exactly on)
singular point (
w_R, then there
present example
the line $w = w_R$

The action p
which passes ar
a trajectory joi
branch of the u
rest point. This
outside it—thus
not find graded

This case als
there are three s
is unstable. In f
none of which i

Next, we tune
we know that t
creases, and the
means that the
"saddle node bi
loop, a limit cyc

intersecting three times. As determined by linear stability theory, the singular points are the stable rest state (**R**), and unstable saddle point threshold (**T**), and an unstable spiral (**U**). The system is excitable, with the lower state being a globally attracting rest state: initial conditions near R lead to a prompt decay to rest, while larger stimuli lead to an action potential—a long trajectory about the phase plane. The phase plane portrait moreover reveals that this case of excitability indeed has a distinct threshold which is due to the presence of the saddle point, T. To understand this, we note that associated with the saddle are a unique pair of incoming trajectories (bold dashed lines) corresponding to the negative eigenvalue of the Jacobian matrix; together, these represent the *stable manifold.* Corresponding to the positive eigenvalue are a pair of trajectories (bold lines) that enter the saddle as $t \to -\infty$; these are the *unstable manifold.* (XPP has a command that generates these manifolds.) The stable manifold defines a separatrix curve in the phase plane that sharply distinguishes sub- from superthreshold initial conditions. For initial conditions near the threshold separatrix, there is a long latency before a firing or decaying subthreshold response (see figure 7.4A). This is because the trajectory starts close to (but not exactly on) the stable manifold and thus the solution comes very near the saddle singular point (where it moves very slowly) before taking off. If w is started at rest, w_R, then there is a unique value of $V = V_T$ (between -22.1 and $-22.2\,\mathrm{mV}$ in the present example) called the "voltage threshold," where the stable manifold intersects the line $w = w_R$.

The action potential trajectory follows along the unstable manifold (bold lines), which passes around the unstable spiral and eventually tends to the rest point. Such a trajectory joining two singular points is called a "heteroclinic orbit." The other branch of the unstable manifold is also a heteroclinic orbit from the saddle to the rest point. This heteroclinic pair forces any trajectory that begins outside it to remain outside it—thus preserving the amplitude of the action potential. In this case we do not find graded responses for any brief current pulses from the rest state.

This case also provides a counterexample to the common misconception that if there are three steady states, then the "outer" two are stable, while the "middle" one is unstable. In fact, in some parameter regimes this model has three singular points, none of which is stable.

Next, we tune up I and ask when repetitive firing occurs. Because I_{ss} is N-shaped, we know that the lower and middle values of $\bar{V}$ move toward each other as I increases, and there is a critical value I_1 where they meet. In the phase plane, this means that the rest point and the saddle coalesce and then disappear; this is called a "saddle node bifurcation." Moreover, the heteroclinic pair become a single closed loop, a limit cycle, which for I just above I_1 has very long period (figure 7.5). Thus,

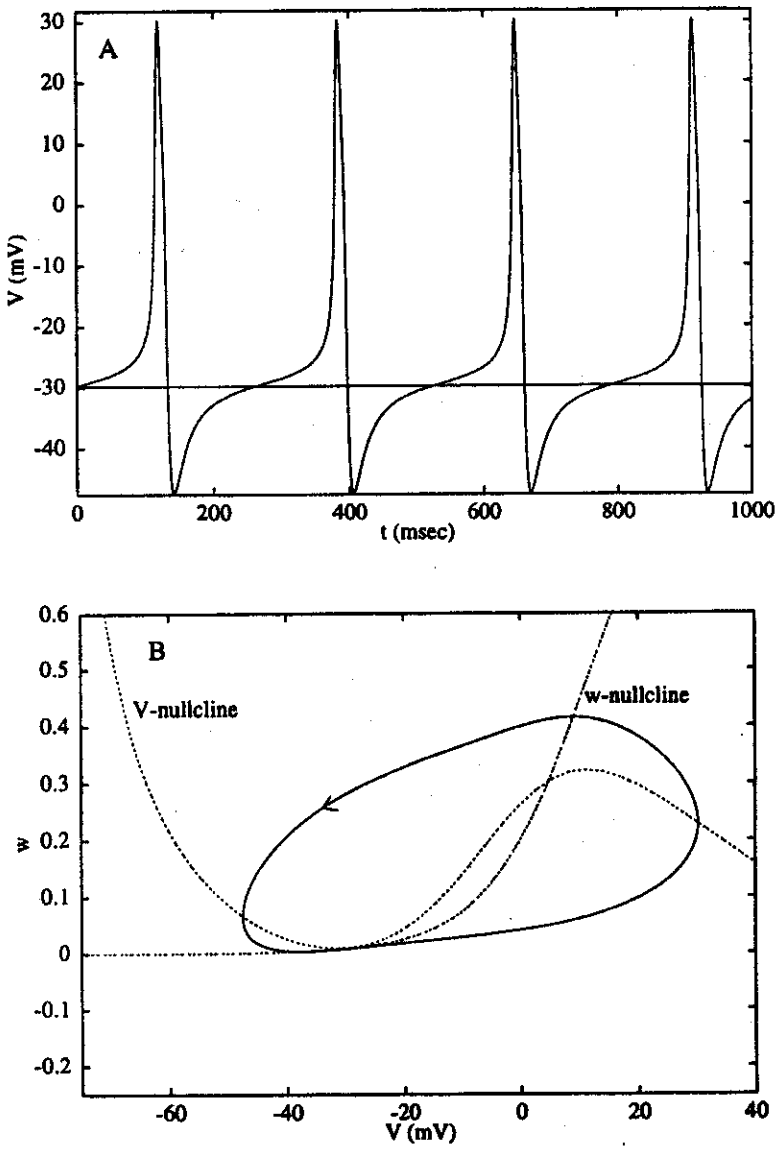

Figure 7.5
Onset of repetitive firing with arbitrarily low frequency for a constant current, $I = 40.76\,\mu A/cm^2$ shows an oscillation with a period of about 220 msec. Panel A shows the voltage time course and panel B shows the phase plane. Note the "narrow channel" between the two nullclines near -30 mV, which accounts for most of the oscillation period (see Rinzel and Ermentrout 1989). Parameters are as in figure 7.4.

in this parameter regime, the transition to repetitive firing is marked by arbitrarily low frequency (figure 7.6B). For I near the critical current, the frequency is proportional to $\sqrt{I - I_1}$ (Strogatz 1994). When $I = I_1$, the limit cycle has infinite period; it is called a "saddle node loop" or SNIC (saddle node on an invariant circle). Generally, an infinite period limit cycle is called a "homoclinic orbit," one that begins and ends at a singular point. The saddle node loop is one type of homoclinic orbit; we will encounter another type in the next section. This type of zero-frequency onset is generic and occurs over a range of parameters. Changing another parameter will typically lead to a smooth change in I_1. We emphasize that this mechanism allows arbitrarily low firing rates without relying on channel gating kinetics, which are necessarily slow. Such low rates have been associated with the inactivating potassium A-type current (Connor, Walter, and McKown 1977), although the underlying mathematical structure of the saddle node loop does not, of course, require an A-current (Rush and Rinzel 1995). We have found the fast spike dynamics in several recent models (e.g., Traub et al. 1991) for cortical pyramidal cells to have this same zero-frequency onset of repetitive firing (unpublished observations by the authors). The value I_1 is determined by evaluating I_{ss} at the value of V for which $\partial I_{ss}/\partial v = 0$, and this latter condition is equivalent to having the determinant $ad - bc$ of the Jacobian matrix equal zero.

The global picture of repetitive firing is shown in the bifurcation diagram of figure 7.6A, with frequency versus I in figure 7.6B. The branch of steady states (unstable shown dashed) form the S-shaped curve, and the oscillatory solutions are represented by the forked curve whose open end begins at $I = I_1$. As I increases beyond I_1 the peak-to-peak amplitude on the stable (repetitive firing) branch decreases and the frequency increases. The family of periodic solutions terminates at $I = I_2$ via a subcritical Hopf bifurcation. Except for I in a small interval of this upper range, this system is monostable. Annihilation of repetitive firing, as in figure 7.3, cannot be carried out for I near I_1 in this case (although at the high-current end where there is bistability, annihilation can occur).

7.3.4 More Bistability

It is important to realize that the solution behavior we have described in our bifurcation diagrams depends on other parameters in the model. The temperature parameter ϕ is particularly convenient, with useful interpretative value for additional parametric tuning: it plays no role in I_{ss} and thus does not affect the values along the S-shaped curve of steady states in figure 7.6, or the corresponding curve in figure 7.2. The *stability* of a steady state does, however, depend on ϕ. As is seen from eq. 7.19,

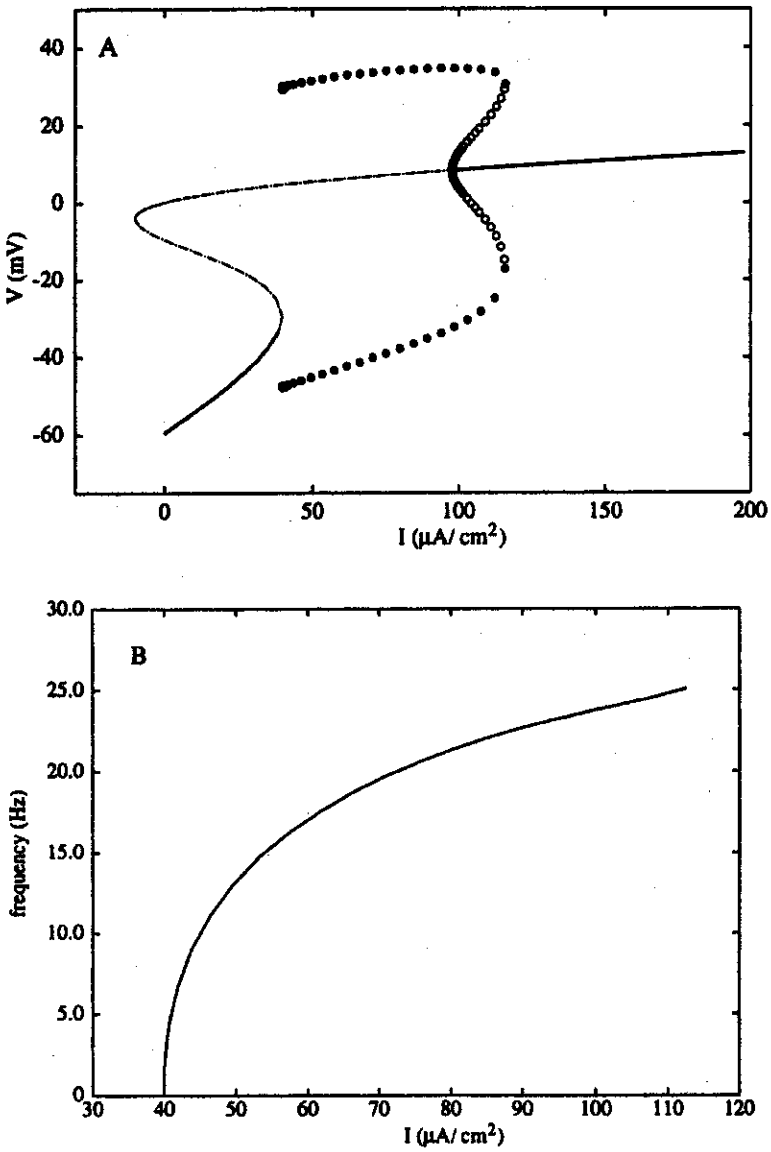

Figure 7.6
Multiple steady states and periodic orbits for a steady current when the I_{ss}–V relation is N-shaped. (A) Bifurcation diagram (line types as in figure 7.2A; parameters are as in figures 7.4–7.5). In spite of the coexistent states, the system is monostable for I between $I_1 = 40$, the turning point of the steady states, and $I_2 = 98$ where there is a Hopf bifurcation. Onset of repetitive firing at zero frequency occurs at $I = I_1$ where two fixed points coalesce. This corresponds to figure 7.4B when the unstable manifolds of the saddle point form a closed loop. The branch of periodic orbits has a turning point at $I = 116$ before terminating at the Hopf bifurcation point, $I = I_2$. All current values in μA/cm^2. (B) Frequency (in Hz) of stable branch of periodic orbits.

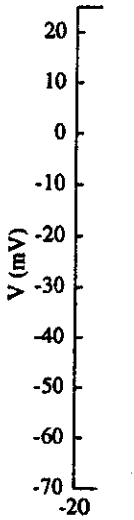

Figure 7.7
Bifurcatio
coalesce,
of the sta
solutions
homoclini
(2) a high
that of fig
Vertical li

when ϕ
steady s
Thus, fo
middle
kinetics
that the
only by
unstable
venientl
ences be
For i
and the
furcatio

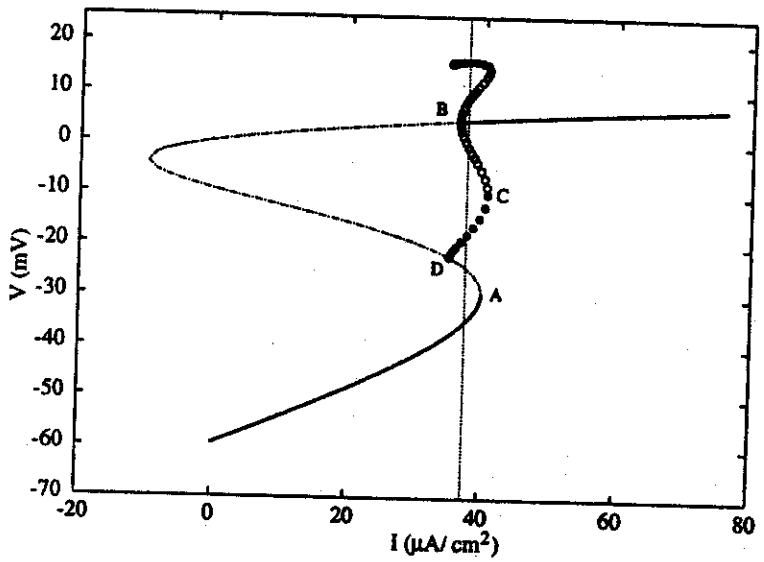

Figure 7.7
Bifurcation diagram (as in figure 7.6 but for $\phi = 0.23$). Point A shows where the two lower steady states coalesce, point B shows the Hopf bifurcation for the upper steady state, point C shows the coalescence of the stable and unstable periodic branches, and point D shows where the branch of stable oscillatory solutions terminates on the branch of saddle points (not on the knee, as in figure 7.6) at a saddle loop homoclinic. For currents between points B and A, there are three stable states: (1) a low-voltage rest state, (2) a high-voltage rest state, and (3) an oscillatory state. Note that the steady-state branch is identical to that of figure 7.6; ϕ only affects the stability of the steady states and the behavior of the periodic orbits. Vertical line at $I = 37.5\,\mu A/cm^2$ shows a current for which there are three stable states (cf. figure 7.8).

when ϕ is large, oscillatory destablization is precluded; Hopf bifurcation from a steady state only occurs when the time scale of w is slow compared to that of V. Thus, for large ϕ, both the upper and lower branches of the S-curve are stable; the middle branch is of course unstable. This system is bistable. In this large-ϕ limit, the kinetics of the K^+ system are so fast (essentially instantaneous, with $w = w_\infty(V)$) that the model reduces to one dynamic variable, V. Then stability is determined only by the slope of I_{ss}, with the two "outer" states being stable and the "middle" unstable. This simple example also shows that sometimes a model can be conveniently reduced to a lower dimension when there are significant time scale differences between variables.

For intermediate values of ϕ, the dynamics of both V and w influence stability, and the upper branch is unstable for a certain range of I. Figure 7.7 shows a bifurcation diagram analogous to that in figure 7.6A, in which the branch of steady

states is S-shaped and the stable rest state disappears at a turning point (point A). The high voltage equilibrium is stable for large currents but, as the current is reduced, loses stability at a subcritical Hopf bifurcation (point B). An unstable branch of periodic solutions emanates from the Hopf bifurcation point and then becomes stable at a turning point (C). Unlike figure 7.6A, however, this branch of stable periodic orbits (solid circles) does not terminate on the knee (point A) but instead on the unstable middle branch (point D on the diagram) as the current decreases to a critical value, I_D. Again the frequency of the limit cycle tends to zero for this branch, but not as the square root. Rather, the frequency is proportional to $1/|\log(I - I_D)|$ (Strogatz 1994). At the critical value of current, I_D, the closed orbit has infinite period; it is called a "saddle loop homoclinic orbit." Recall that the middle branch of solutions is a saddle point. One branch of the unstable manifold of this saddle point exits the singular point and returns via a branch of the stable manifold (compare figure 7.8A) and contrast this with the saddle node loop homoclinic in figures 7.4–7.6). For certain values of the current, this system is *tristable*, that is, it has three stable states. If I is chosen to lie between the I values for points B and C, then the lower branch still exists and is stable, the upper branch of equilibria is stable, and there is a stable periodic orbit. Figure 7.8A shows the phase plane for this case. The stable manifold for the saddle point (bold dashed trajectory) acts to separate the stable periodic orbit (SPO) from the lower rest state. The small unstable periodic orbit (UPO) separates the upper rest state from the stable periodic solution. As in figure 7.3B, we can use brief current pulses to switch between states. Figure 7.8B shows the effect of three 5 msec current pulses switching from the periodic orbit to the lower rest state, back to the periodic orbit, and then to the upper rest state. (Note that perturbations from the upper rest state decay very slowly.) The HH model, adjusted for higher than normal external potassium, exhibits similar multistable behavior (Rinzel 1985).

This example of coexistence between a depolarized limit cycle and a lower resting state is important because it also forms the basis for a general class of bursting phenomena.

7.4 Bursting and Adaptation: Spiking Dynamics with Slow Modulation

Many neurons exhibit much more complicated firing patterns than the simple repetitive firing we have described here. *Bursting*, the clustering of spikes followed by relative quiescence, is a common mode of firing in neurons and other excitable cells (see Wang and Rinzel 1995 for a brief review). Bursting cannot happen in two-variable

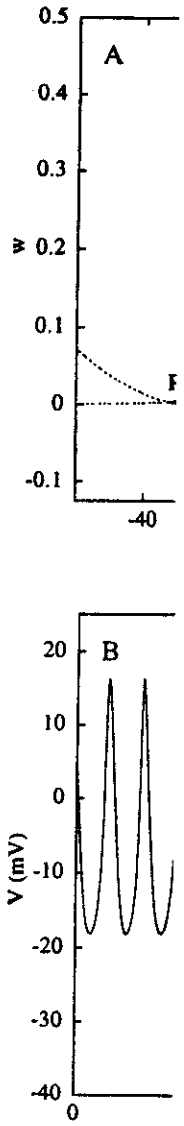

Figure 7.8
Multistability for . as in figure 7.7). P steady states: (1) a state (unlabeled). ' lower steady state stable manifold of and the stable per from the stable pc Starting on the sta pulse pushes it ba single brief curren though the opposi

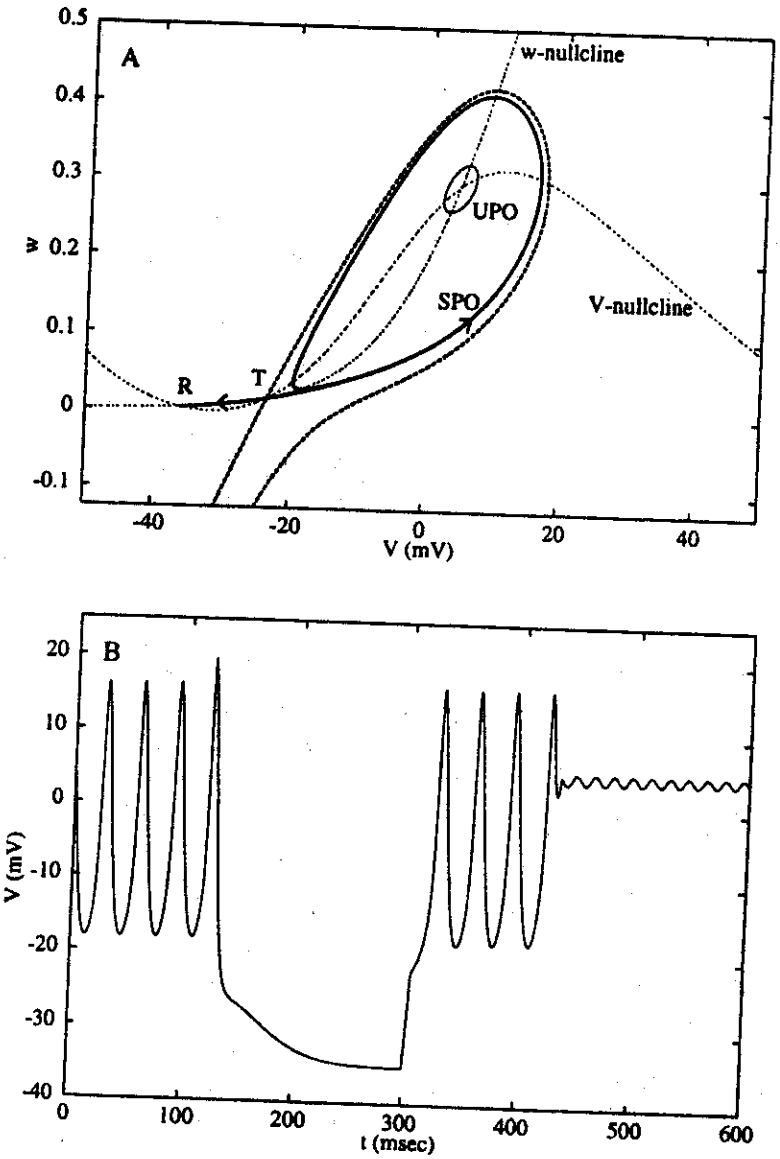

Figure 7.8
Multistability for a current between points B and A in figure 7.7 ($I = 37.5\,\mu A/cm^2$; other parameters are as in figure 7.7). Panel A depicts the V-w phase plane. The nullclines intersect at three places representing steady states: (1) a lower stable rest state (R), (2) an unstable saddle point (T), and (3) an upper stable rest state (unlabeled). The left branch of the unstable manifold of the saddle point (bold line) connects to the lower steady state. The right branch wraps around the stable periodic orbit (SPO). The branches of the stable manifold of the saddle point (bold dashed line) form a separatrix between the lower stable rest state and the stable periodic orbit. The unstable periodic orbit (UPO) separates the stable upper steady state from the stable periodic orbit. Panel B shows the effects of three successive depolarizing current pulses. Starting on the stable oscillation, the membrane is switched to the lower stable steady state. Another brief pulse pushes it back to the stable oscillation and a third pulse switches it to the upper steady state. No single brief current pulse can switch it from the lower steady state directly to the upper steady state, although the opposite transition is possible.

models. The slow modulation of spiking during a burst requires additional biophysical mechanisms and dynamic variables. Moreover, just from mathematical considerations, a slowly drifting spike trajectory that recurs would violate the rule that trajectories in the phase plane cannot cross. By adding a slow process to our idealized two-variable model, however, we can use it to understand bursting from a simple geometric point of view. In this treatment, a slow variable is first viewed as a parameter to describe the behavioral regimes of the fast spike-generating kinetics; the slow dynamics are then overlaid as the full system sweeps through regimes of spiking and quiescence. Unless we state otherwise, bursting for us will imply repetitive bursting.

7.4.1 Square-Wave Bursters

Consider in figure 7.7 the I interval between A and D. There is a stable rest state around $-35\,\mathrm{mV}$ and a stable (more depolarized) limit cycle. Suppose the current I slowly varies back and forth across this interval. Then because of the bistability, a hysteresis loop is formed, in which the membrane is alternately at rest and alternately firing repetitively. Such a loop provides a simple mechanism and geometric interpretation for *square-wave bursting*. Because the current I is externally imposed, however, this is forced rather than autonomous bursting. To achieve autonomous bursting, one could (as in Rinzel and Ermentrout 1989) redefine I as a dynamic dependent variable in such a way that I decreases when the membrane is depolarized and firing repetitively, and I increases when the membrane is resting. Although artificial, this example demonstrates the basic principle that (very) slow negative feedback and hysteresis in the fast dynamics underlie square-wave bursting. Many different ionic current mechanisms could likewise produce the slow negative feedback. For further illustration, we employ a calcium-dependent potassium current, analogous to that studied by others (see Wang and Rinzel 1995). We assume the current activates instantaneously in response to calcium and that the calcium-handling dynamics are slow. Thus we add to eq. 7.6 the current I_{K-Ca} given by

$$I_{K-Ca} = g_{K-Ca} z (V - V_K), \tag{7.20}$$

where g_{K-Ca} is the maximal conductance for this current and z is the gating variable with a Hill-like dependence on Ca (the near-membrane calcium concentration scaled by its dissociation constant for activating the gate, K_D):

$$z = \frac{Ca^p}{Ca^p + 1}. \tag{7.21}$$

(For simplicity, we set the Hill exponent $p = 1$, although this is not required.) The balance equation for Ca is

$$\frac{dCa}{dt} = \varepsilon(-\mu I_{Ca} - Ca), \tag{7.22}$$

where the parameter μ is for converting current into a concentration flux and involves the ratio of the cell's surface area to the calcium compartment's volume. The parameter ε is a product of the calcium removal rate and the ratio of free to total calcium in the cell. Because calcium is highly buffered, ε is small and thus the calcium dynamics are slow. This is a greatly simplified model; one could have, for example, more complicated calcium handling, including diffusion of calcium in the cytoplasm, nonlinear removal of calcium by pumps/exchangers, perhaps even release of calcium from intracellular pools. If the conductance g_{K-Ca} of this outward current is large, the membrane is hyperpolarized; if it is small, then the membrane can fire. Thus, when a bifurcation curve is drawn as a function of this conductance, it is reversed from that of figure 7.7, which plots the behavior as a function of an *inward* current. When the membrane is firing, intracellular calcium slowly accumulates, turning on this outward conductance and thereby terminating the firing. Figure 7.9A shows a bursting solution to the three-variable model, eqs. 7.4–7.6 coupled with the slow calcium dynamics, eq. 7.22. Projecting the solution onto the z-V plane, where z is defined in eq. 7.21, shows how the burst's trajectory slowly tracks the attracting branches of the fast subsystem (figure 7.9B). Rapid transitions occur when the branches terminate at bifurcation points and turning points. We note that any number of alternate mechanisms could provide the slow negative feedback for bursting including a slow gating kinetics for z with fast calcium handling, or slow inactivation of I_{Ca}, driven by V or Ca.

7.4.2 Chaos and Poincaré Maps

We emphasize that even our minimal three-variable model exhibits the complex dynamics of bursting oscillations. Moreover, because of its simplicity and the geometric viewpoint we offer, the role of each variable is clear; V and w are for fast spike generation with bistability, and Ca provides the slow modulation. Finally, the model is sufficiently robust that in certain parameter ranges, it appears to exhibit chaotic behavior. Increasing the K_D for the calcium-dependent potassium conductance, equivalent to decreasing μ, can switch the membrane into a repetitively firing regime. The transition between the bursting and repetitive regimes is very complicated. For example, when $\mu = 1/59$, the burst pattern has period 4, that is, every fourth burst is the same. When $\mu = 1/60$, behavior is aperiodic (time course not shown); its

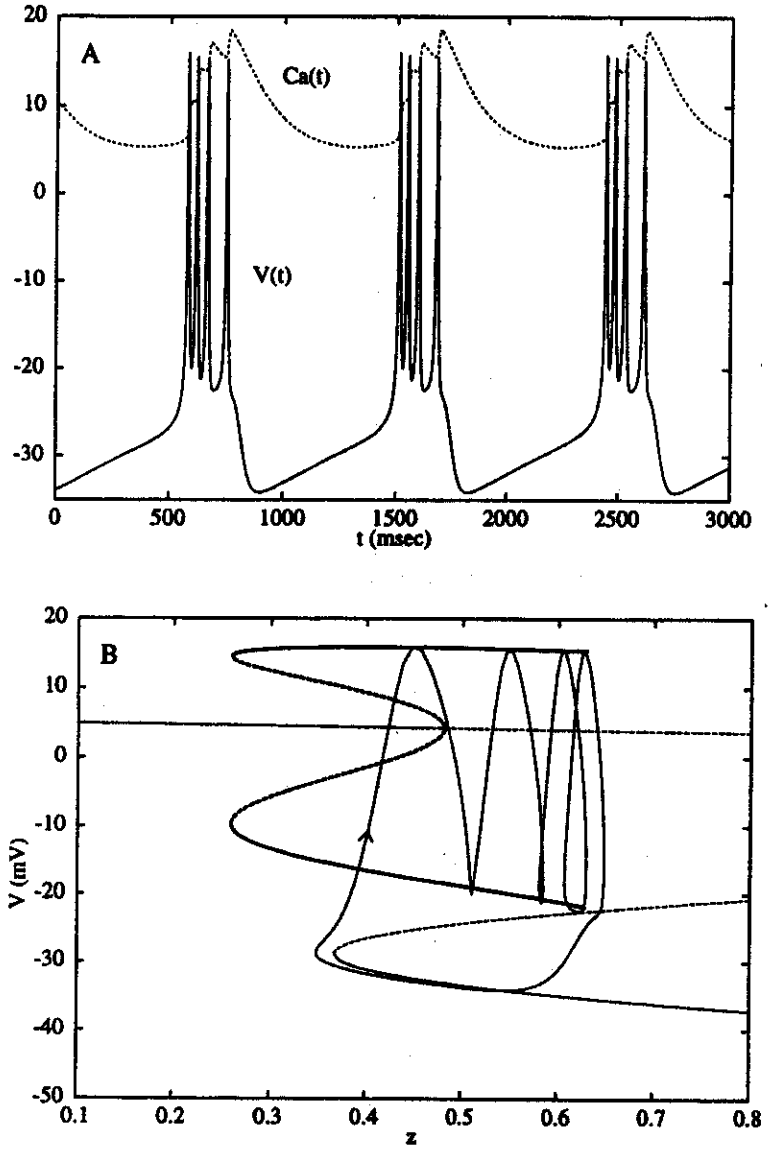

Figure 7.9
Bursting solution to eqs. 7.4–7.6 coupled with the calcium-dependent potassium current, eqs. 7.20–7.22. Parameters are as in figure 7.7, with $I = 45\,\mu A/cm^2$, $\varepsilon = 0.005$, $\mu = 0.2$, $g_{K-Ca} = 0.25\,mS/cm^2$. Panel A shows the voltage trace (use mV for ordinate scale) and the calcium concentration (for plotting clarity, the dimensionless Ca values have been multiplied by ten; ordinate scale is unitless in this case). The burst's active phase ends when calcium rises too high and the membrane hyperpolarizes. During the silent phase calcium is removed and after the calcium-dependent potassium current diminishes enough the membrane depolarizes to initiate the next burst. Panel B shows the projection of the bursting solution on the z-V plane along with the bifurcation diagram with $z = Ca/(1 + Ca)$ as a parameter. The trajectory alternately tracks the stable periodic solution (SPO in figure 7.8A) and the lower steady state. Panel C shows that for a slightly different value, $\mu = 0.01667$, the solution is chaotic; data points plot the value of calcium at successive times as the voltage decreases through 0 mV. The solid diagonal line is the identity function.

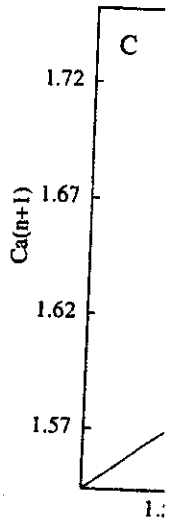

Figure 7.9 (contin

dynamics can
when V decrea
the value of w.
The value of c
proximately rep
can generate th
series as follow
calcium, and th
getting the next
to a new value
dynamics of ou
shown in figure
line $y = x$ and y
Ca^*, to which th
solution to the r
solution is unsta
behavior, that is,
By reducing the
iteration, we car
firing to chaos a

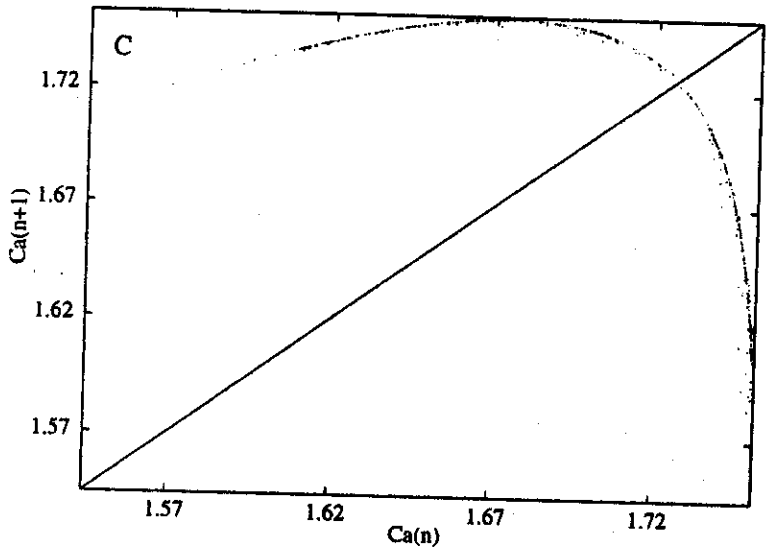

Figure 7.9 (continued)

dynamics can be described as follows. Each time that V passes a given value (here when V decreases through 0 mV), we record the concentration of calcium, as well as the value of w. For this particular model, the recorded values of w are all about 0.35. The value of calcium, however, varies between 1.56 and 1.73. The solution is approximately represented by the time series of values for the calcium, $Ca_1, Ca_2, \ldots$ We can generate the one-variable dynamic rule whose solutions approximate these time series as follows. With initial conditions $V = 0$ and $w = 0.35$, we specify a value for calcium, and then integrate the full differential equations until V crosses 0, again getting the next value of calcium. Thus we have a *map* taking a value of calcium, Ca, to a new value of calcium, $F(Ca)$. This map is called a "Poincaré map." The entire dynamics of our burster are captured by this simple map. For $\mu = 1/60$, this map is shown in figure 7.9C. From the figure, it is evident that there is an intersection of the line $y = x$ and $y = F(x)$. That means that there is a single concentration of calcium, Ca^*, to which the trajectory returns after one cycle. This corresponds to a periodic solution to the model equations. If $|F'(Ca^*)| > 1$ (as is the case here), the periodic solution is unstable. This type of map is characteristic of dynamics that have *chaotic behavior*, that is, the successive values of calcium appear to be random and aperiodic. By reducing the three-dimensional differential equation to a simple one-dimensional iteration, we can understand the essence of the transition from constant repetitive firing to chaos as we vary a parameter, say μ. (More details on one-dimensional

maps and chaos can be found in Glass and Mackey 1988; for an application to a neuronal bursting system, see Hayashi and Ishizuka 1992.)

7.4.3 Elliptic Bursters

Bursting that differs from the square-wave pattern above can arise from slow modulation of bistable fast dynamics because bistability can arise in a number of ways. Consider a parameter regime for eqs. 7.4–7.6 in which the onset of oscillations is via a subcritical Hopf bifurcation, such as shown in figures 7.2 and 7.3. As for the square-wave burster, there is a regime where the spike-generating dynamics are bistable; a limit cycle and a fixed point coexist, although, unlike the bistability shown in figure 7.7, the limit cycle "surrounds" the fixed point. Figure 7.10 shows an example of an "elliptic burst" pattern generated when the fast dynamics of figures 7.2 and 7.3 are coupled with the slow calcium-dependent potassium current used in the previous bursting model (eq. 7.22). In figure 7.10A, the envelope of the spikes is "elliptical" in shape as the amplitude gradually waxes and wanes. The silent phase is characterized by damping and growing oscillations as the trajectory slowly drifts through the Hopf bifurcation of the fast subsystem. This type of activity pattern has been seen in sleep spindles, and a cellular model related to it involves the same mathematical mechanism (Destexhe, McCormick, and Sejnowski 1993; see also Wang and Rinzel 1995, and Rush and Rinzel 1995). As with a square-wave burster, this type of bursting can also have complex dynamics such as quasi-periodic behavior and chaos.

7.4.4 Parabolic Bursting: Two Slow Processes

Bursting can arise even without bistability in the spike-generating dynamics. Minimal models for the most widely known endogenous cellular burster, the *Aplysia* R-15 neuron, operate in a regime where the fast dynamics are monostable (Rinzel and Lee 1987). Suppose the spiking dynamics are as in figures 7.4–7.6, where the onset of repetitive firing is through a saddle-node-loop bifurcation and there is no bistability. (Ignore the bistable behavior at high currents. We are interested in the low-current regime only, where the rest state is more negative than $-30\,\mathrm{mV}$.) The mechanisms for bursting that depend on *one* slow variable cannot produce bursting in this parameter regime because there is no longer a hysteresis loop. A model with a single slow variable interacting with these fast dynamics will, in response to a steady input, slowly approach a maintained state of repetitive firing or rest. The slow transient phase for a depolarizing input could show increasing or decreasing activity depending on whether the slow variable provides positive or negative feedback. Figure 7.11A illustrates that $I_{K\text{-}Ca}$ with slow Ca dynamics provides a mechanism for adaptation in repetitive firing behavior.

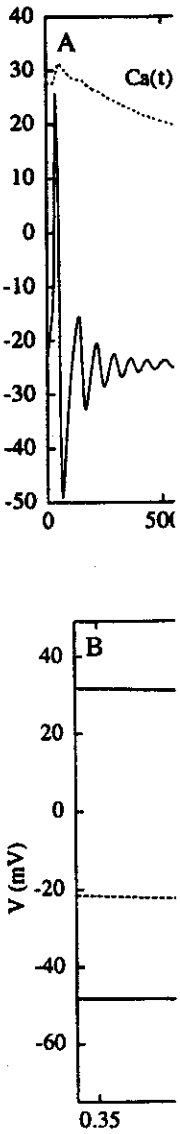

Figure 7.10
Elliptic burster for
7.2, is coupled t
in figure 7.2, with
courses of voltage
high and the calci
calcium is low en
figure 7.9B. Durin
subsystem. Actual
regime of the fast

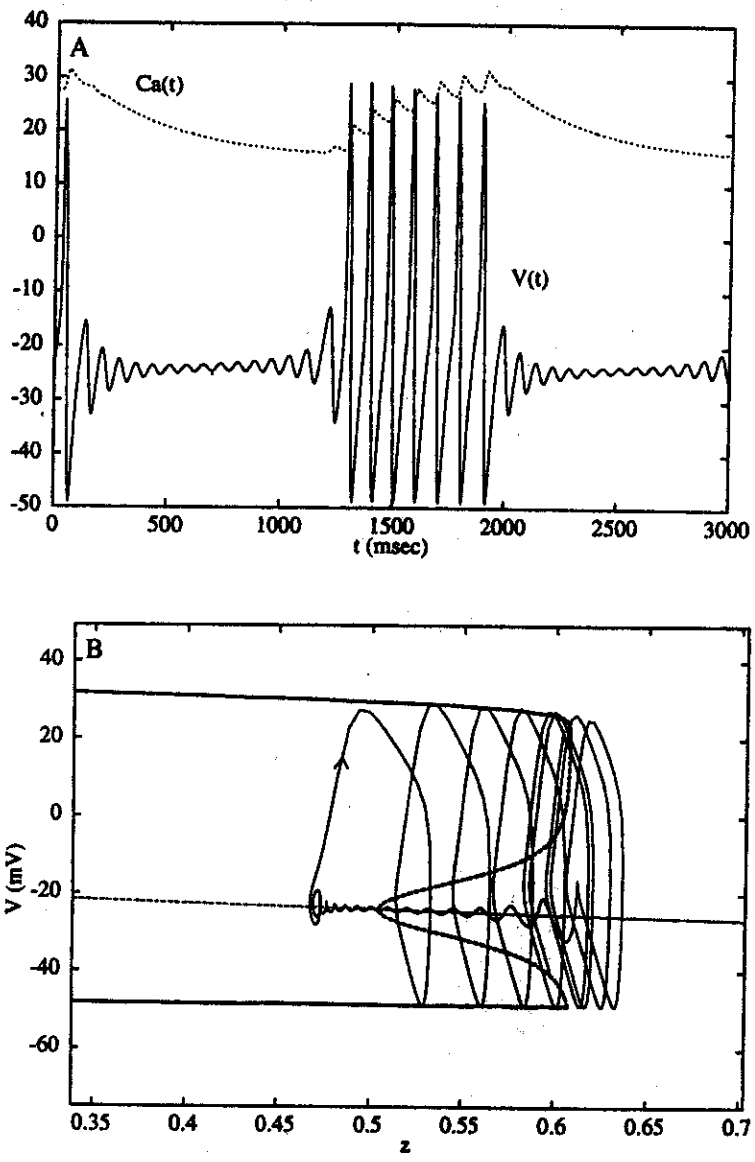

Figure 7.10
Elliptic burster formed when the Morris-Lecar model, equations 7.4–7.6 in the parameter regime of figure 7.2, is coupled to the calcium-dependent potassium current, equations 7.20–7.22. Parameters are as in figure 7.2, with $I = 120\,\mu A/cm^2$, $\mu = 0.3$, $\varepsilon = 0.002$, $g_{K\text{-}Ca} = 0.75\,mS/cm^2$. Panel A shows the time courses of voltage and calcium (ordinate scales as in figure 7.9A). As in figure 7.9, when the calcium is high and the calcium-dependent potassium channel is activated, the membrane tends toward rest; when calcium is low enough, it is oscillatory. Panel B shows the projection of the burst on the z-V plane as in figure 7.9B. During the active and silent phases, the burst trajectory slowly tracks attractors of the fast subsystem. Actually during the later phase of the silent period, the trajectory drifts well into the unstable regime of the fast subsystem's rest state (left of the Hopf point, $z < 0.5$), and this feature is explainable.

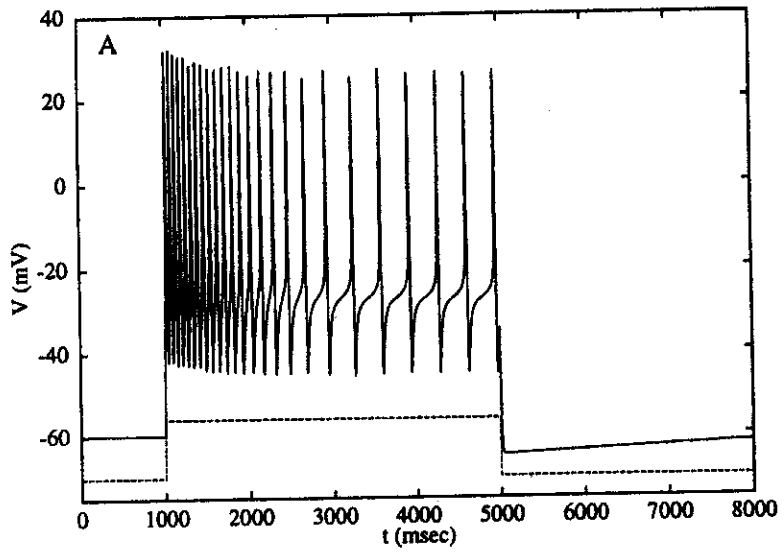

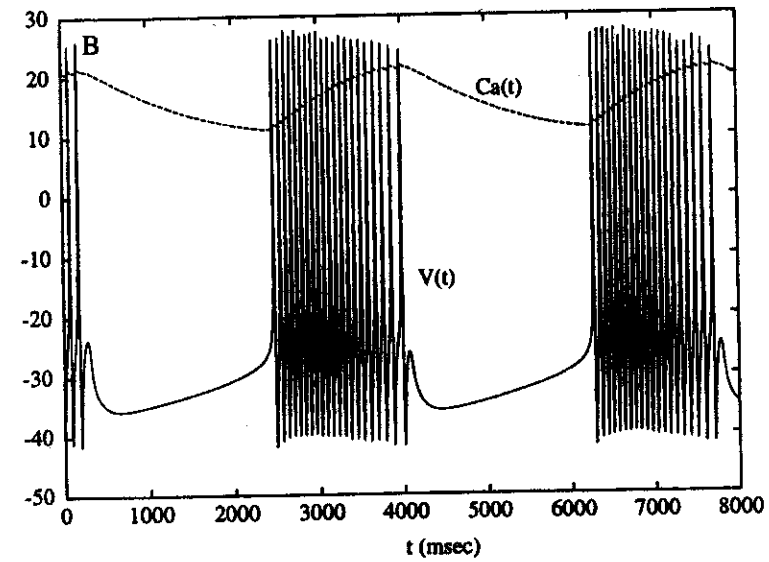

Figure 7.11
Modulation of the Morris-Lecar model, equations 7.4–7.6 in the regime of figure 7.4, by slower processes. Panel A shows how coupling with the calcium-dependent potassium current, eqs. 7.20–7.22, results in adaptation to a long current pulse. Parameters are as in figure 7.4, with $g_{K\text{-}Ca} = 1\,\mathrm{mS/cm^2}$, $\mu = 0.025$, $\varepsilon = 0.0005$. The current pulse is $70\,\mu\mathrm{A/cm^2}$. The membrane initially fires repetitively at 17 Hz and eventually slows to 3 Hz, more than a fivefold decrease. Panel B shows that a parabolic burster is formed by adding an additional slow inward current governed by eq. 7.23 with $I = 65\,\mu\mathrm{A/cm^2}$, $g_{Ca,s} = 1\,\mathrm{mS/cm^2}$, $\tau_s = 0.05\,\mathrm{msec}$. Other parameters are as in panel A. This plot shows the membrane potential and the dimensionless calcium concentration as functions of time (ordinate scales as in figure 7.9A). For plotting convenience, Ca has been multiplied by ten. Panel C shows the projection of the burst onto the z-s plane. The dashed line is the curve of saddle-node-loop bifurcations of the fast dynamics, viewing s and z as parameters. Above this line, the membrane is oscillatory; below it, there is only a stable rest state.

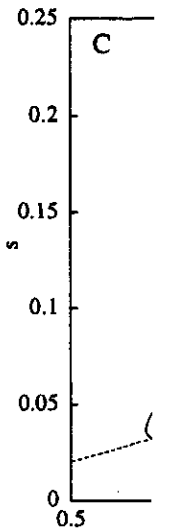

Figure 7.11 (cor

To obtain
another slow
catalytic) an
current to th
rent slowly a
on the slow
for the slow
repeats. Thu
produce slov
firing regime
able with an
Rinzel and I
and Carrillo

To illustra
only add a s
an additiona

$I_{Ca,s} = g_{Ca,s}s$

where

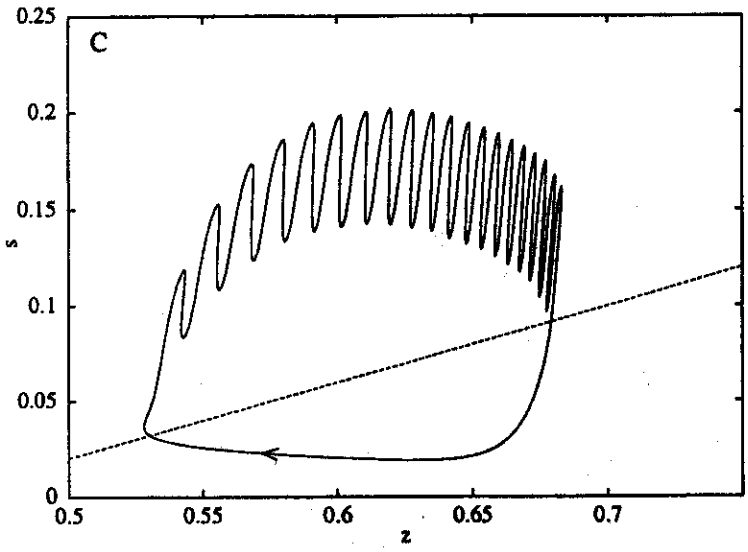

Figure 7.11 (continued)

To obtain the slow oscillation that underlies parabolic bursting, we need yet another slow variable so that there are opposing influences of slow positive (autocatalytic) and slow negative feedback. Suppose, therefore, that we add a slow *inward* current to the model, which means there are two slow variables. As the inward current slowly activates, it causes the membrane to fire repetitively; this, however, turns on the slow outward current, which then shuts the membrane down. If the threshold for the slow inward current is low enough, it can start up once again and the process repeats. Thus a combination of a slow outward current and slow inward current can produce slow oscillations that move the fast dynamics into and out of the repetitively firing regime. The generality of this mechanism for parabolic bursting (also realizable with an inward current that slowly activates and then slowly inactivates, as in Rinzel and Lee 1987) has been described by a number of authors (e.g., Baer, Rinzel, and Carrillo 1995).

To illustrate with the Morris-Lecar model (that includes $I_{K\text{-}Ca}$ as above), we need only add a slow autocatalytic process. With considerable freedom of choice, we add an additional slowly activating calcium current:

$$I_{Ca,s} = g_{Ca,s}s(V - V_{Ca}),$$

where

$$\tau_s \frac{ds}{dt} = \varepsilon(s_\infty(V) - s). \tag{7.23}$$

For simplicity, we have chosen $\tau_s = 0.05$ as a constant and

$$s_\infty(V) = 0.5[1 + \tanh(V - 12)/24].$$

Figure 7.11B shows the voltage trace of the burst pattern. Note how the interspike interval is relatively longer at the beginning and end of each burst. Figure 7.11C shows the projection of the two slow gating variables, s and z, during a burst. The dashed line represents the boundary between fixed points and oscillation for the fast dynamics when the slow variables are held fixed; it is where the saddle-node-loop bifurcation occurs. Above this line, the fast dynamics are oscillatory and below it, there is a unique stable fixed point.

We have shown how modulating the various types of fast dynamics with one or two slow processes leads to simple mechanisms for generating several different types of bursting oscillations. This geometric viewpoint lets us dissect the mechanisms that underlie some complex neuronal bursting dynamics. Other factors can contribute to burst rhythmogenesis including cable properties and spatially nonuniform channel densities, and nonlinear regenerative factors in the calcium handling system (cf. Wang and Rinzel 1995).

7.5 Phase-Resetting and Phase-Locking of Oscillators

We now turn our attention to a brief description of periodically forced and coupled neural oscillators. The behaviors generally involve issues that are very difficult to analyze and we will only touch on them briefly. Before treating a specific example, it is useful to discuss certain important aspects of oscillators. We say that a periodic solution to an autonomous (time does not explicitly appear in the right-hand side) differential equation is (*orbitally*) "asymptotically stable" if perturbations from the oscillation return to the oscillation as $t \to \infty$. The difference between asymptotic stability of an oscillation and that of a steady-state solution is that, for the oscillation, the time course may exhibit a shift. That is, we do not expect the solution of the perturbed oscillation to be the same as the unperturbed; rather, there will be a shift (see figure 7.12A) due to the time translation invariance of the periodic solution. Indeed, in phase space, the periodic trajectory is unchanged by translation in time. The shift that accompanies the perturbation of the limit cycle can be exploited in order to understand the behavior of the oscillator under external forcing. Suppose that an oscillator has a period, say T. We may let $t = 0$ correspond to the time of

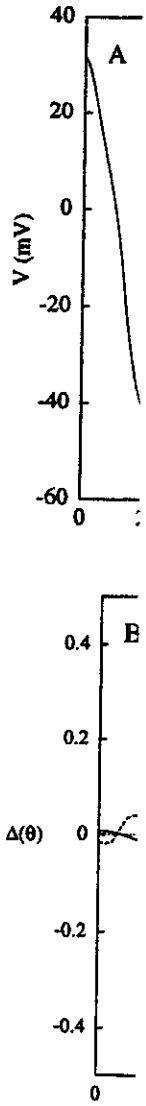

Figure 7.12
Phase-resetting
next spike and
with paramete
pulse with amp
depolarizing st
responds to the

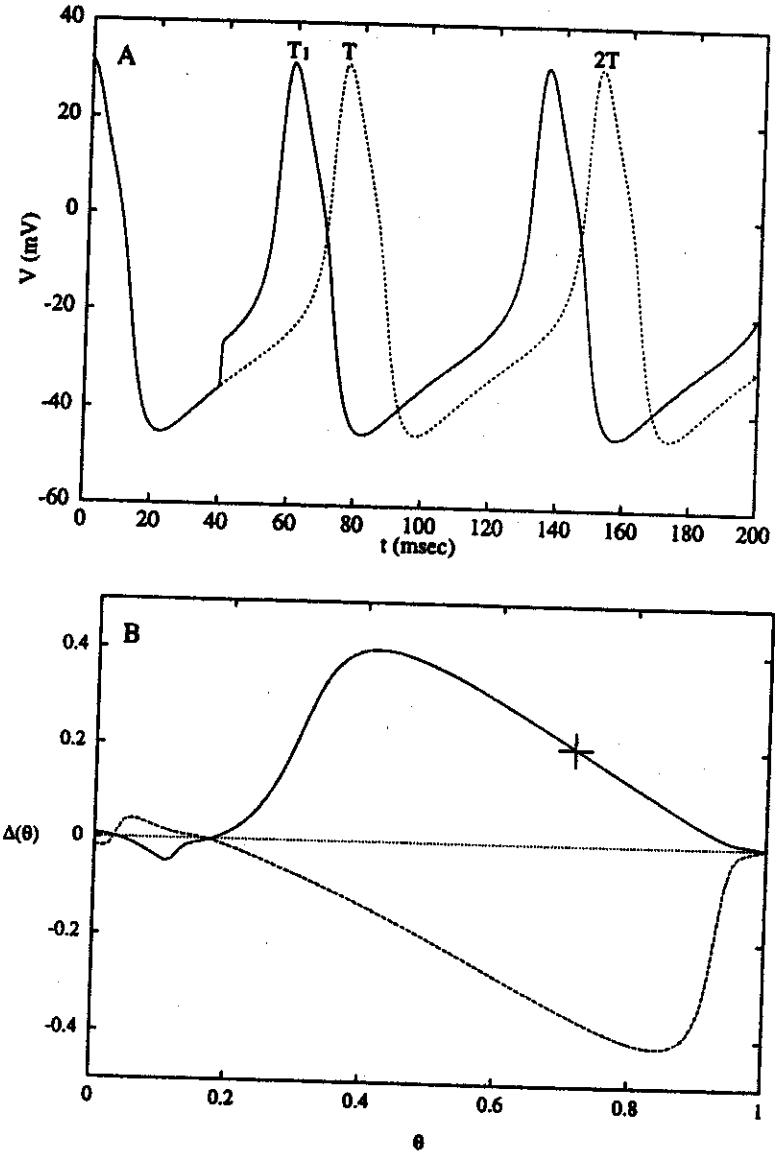

Figure 7.12
Phase-resetting of a Morris-Lecar oscillator. (A) A brief depolarizing stimulus can shorten the onset of the next spike and thus advance the phase. (B) Phase response curve (PRC) for the Morris-Lecar equations with parameters as in figures 7.4–7.6 and an applied current $I = 50\,\mu A/cm^2$. The stimulus is a 0.5 msec pulse with amplitude of $\pm 480\,\mu A/cm^2$ delivered at time $t = 40$ msec. The solid line shows the PRC for a depolarizing stimulus and the dashed for a hyperpolarizing pulse. The cross on the depolarizing PRC corresponds to the experiment in figure 7.13.

peak value of one of the oscillating variables, so that at $t = T$ we are back to the peak. Given that we are on the periodic solution, if some t is specified, then we know precisely the state of each oscillating variable. This allows us to introduce the notion of *phase* of the periodic solution. Let $\theta = t/T$ define the phase of the periodic solution so that $\theta = 0, 1, 2, \ldots$ all define the same point on the periodic solution. For example, if $\theta = 8.5$, then we are halfway through the oscillator's ninth cycle.

7.5.1 Phase Response Curves

With the notion of phase defined, we now examine how a perturbation shifts the phase of the oscillator. In figure 7.12A, we show the voltage time course for the Morris-Lecar system in the oscillating regime. At a fixed time, say t, after the voltage peak, we apply a brief depolarizing current pulse. This shifts the time of the next peak (figure 7.12A) and this shift remains for all time (the solid curve is the perturbed oscillation and the dashed is the unperturbed—in this case the time for the next peak is shortened). If the time of the next peak is shortened from the natural time, we say that the stimulus has "advanced the phase"; if the time of the next peak is lengthened, that we have "delayed the phase." Let T_1 denote the time of the next peak. The phase shift is $(T - T_1)/T$, and T_1 depends on the time t or the phase $\theta = t/T$ at which the stimulus is applied. Thus we can define a phase shift $\Delta(\theta) \equiv (T - T_1(\theta))/T$. The graph of this function is called the "phase response curve" (PRC) for the oscillator. If $\Delta(\theta)$ is positive, the perturbation advances the phase and the peak will occur sooner. On the other hand, if $\Delta(\theta)$ is negative, the phase is delayed and the next peak will occur later. We can easily compute this function numerically, and the same idea can be used to analyze an experimental system. Moreover, this curve can be used as a rough approximation of how the oscillator will be affected by repeated perturbation (periodic forcing) with the same current pulse. (More complete descriptions and numerous examples of phase models and PRCs can be found in Glass and Mackey 1988; Winfree 1980.)

In figure 7.12B, we show a typical PRC for the Morris-Lecar model computed for both a depolarizing stimulus (solid line) and a hyperpolarizing stimulus (dashed line). The stimulus consists of a current pulse of magnitude $480\,\mu A/cm^2$ applied for 0.5 msec at different times after the voltage peak. The time of the next spike is determined, which yields the PRC, as above. The figure agrees with our intuition; if the depolarizing stimulus comes while $V(t)$ is increasing (i.e., during the upstroke or slow depolarization of recovery), the peak will occur earlier and we will see a phase advance. If the stimulus occurs while $v(t)$ is decreasing (i.e., during the downstroke), there will be a delay. The opposite occurs for hyperpolarizing stimuli. The curves show that it is difficult to delay the onset of an action potential with a depolarizing

stimulus or advance it with a hyperpolarizing one. For different sets of parameters, these curves may change. As we have seen in the previous section, it is sometimes possible to completely stop the oscillation if a stimulus is given at the right time. In this case, the PRC is no longer defined; nearby phases can then have arbitrarily long latencies before firing.

We now show how this function can be used to analyze a periodically forced oscillator. Suppose that every P time units a current pulse is applied to the cell. Let θ_n denote the phase right before the time of the nth stimulus. This stimulus will either advance or delay the onset of the next peak depending on the phase at which the stimulus occurs. In any case, the new phase after time P and just before the next stimulus will be $\theta_n + \Delta(\theta_n) + P/T$. To understand this, first consider the case where there is no stimulus: after time P the oscillator will advance P/T in phase, but because the stimulus advances or delays the phase by an amount $\Delta(\theta_n)$, this amount is just added to the unperturbed phase, resulting in an equation for the new phase just before the next stimulus:

$$\theta_{n+1} = \theta_n + \Delta(\theta_n) + P/T. \tag{7.24}$$

This difference equation can be solved numerically. Here we consider the natural question of whether the periodic stimulus can entrain the voltage oscillation. That is, we ask whether there is a periodic solution to this forced neural oscillation. In general, a periodic solution is one for which there are M voltage spikes for N stimuli, where M and N are positive integers. When such a solution exists, we have what is known as "M:N phase-locking."

Finding $M:1$ phase-locked solutions is quite easy. We require the oscillator to undergo M oscillations per stimulus period. In terms of eq. 7.24, this means we seek a solution that satisfies

$$\theta + M = \theta + \Delta(\theta) + P/T \tag{7.25}$$

for some value of θ. If such a solution exists and is stable (to be defined below), then, starting near θ, we can iterate eq. 7.24 and end up back at θ. This θ is the locking phase just before the next stimulus and because it does not change from stimulus to stimulus, the resulting solution must be periodic. Obviously, a necessary condition for a solution to eq. 7.25 is that $M - P/T$ lie between the maximum and minimum of $\Delta(\theta)$, that is, we must solve

$$M - P/T = \Delta\theta. \tag{7.26}$$

Having solved eq. 7.26, we need to determine the stability of the solution. For equations of the form of eq. 7.24, a necessary and sufficient condition for θ to be a stable

solution is that $-2 < \Delta'(\theta) < 0$. Because $\Delta(\theta)$ is periodic and continuous, there will in general be two solutions to eq. 7.26 (see figure 7.12B). But because only one of them will occur where $\Delta(\theta)$ has a negative slope, there will be a unique stable solution. We must also worry about whether the negative slope is too steep (i.e., more negative than -2); for small stimuli, this will never be the case—stability is assured. When $\Delta'(\theta) < -2$ (instability), very complex behavior can occur such as chaos (see, for example, Glass and Mackey 1988). The case of $M : N$ phase-locking where $N > 1$ is more difficult to explain and will not be considered here. It is clear that if the stimulus is weak, the magnitude of $\Delta(\theta)$ will also be small so that $M - P/T$ must be small in order to achieve $M : 1$ locking. On the other hand, if the stimulus is too strong, then we must be concerned with the stability of the locked solution. We note that, in a sense, eq. 7.24 is only valid for stimuli that are weak compared to the strength of attraction of the limit cycle; for stronger stimuli, it will take the solution more than a single oscillation to return to points close to the original cycle. The PRC in figure 7.12B shows that, when the stimulus is depolarizing, it is easier to advance the Morris-Lecar oscillator and thus force it at a higher frequency ($0 < P/T < 1$) than it is to force the oscillator at a lower frequency ($P/T > 1$). For hyperpolarizing stimuli, we can more easily drive the oscillator at frequencies lower than the natural frequency. (The counterresults are possible, but only for small ranges of parameters; see also Perkel et al. 1964)

To illustrate these concepts, we have periodically stimulated the Morris-Lecar model (natural period of 95 msec) with the same brief depolarizing current pulse repeated every 76 msec. Figure 7.13 shows that the oscillation is quickly entrained to the new higher frequency. Equation 7.26 allows us to predict the time after the voltage peak that the stimulus will occur for 1:1 phase-locking. From the PRC we can see that $\Delta(\theta) = 1 - 76/95 = 0.2$ corresponds to two values of θ, one stable (cross in figure 7.12B) $\theta = 0.702$ and the other unstable. Thus the locking time after the voltage peak, that is, when the stimulus occurs, is predicted from the PRC to be $t = T \cdot \theta = 67$ msec. This is exactly the shift observed in figure 7.13.

The technique illustrated here is useful for analyzing the behavior of a single oscillator when forced with a short pulsatile stimulus. For more continuous types of forcing, such as an applied sinusoidal current, other techniques must be used. One such technique is the *method of averaging*, applicable when the forcing is weak. Periodic forcing is a special case of coupling, which we will now describe.

7.5.2 Averaging and Weak Coupling

Although the general behavior of coupled neural oscillators is very difficult to analyze, limiting cases can be treated (Kopell 1988). We will describe one method, the

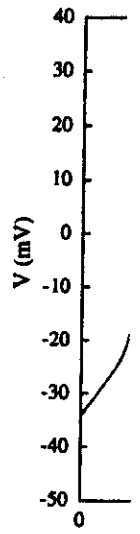

Figure 7.13
Phase-locking
76 msec. Intri
phase-locking
as predicted b

method of
oscillators
trout and K
lator's traje
coupling is
scribed abo
however, th
as averaged
phase-locki
identical m
found in the

We assun
terms of a
period T ar
$j = 1, 2$, and
of coupling,

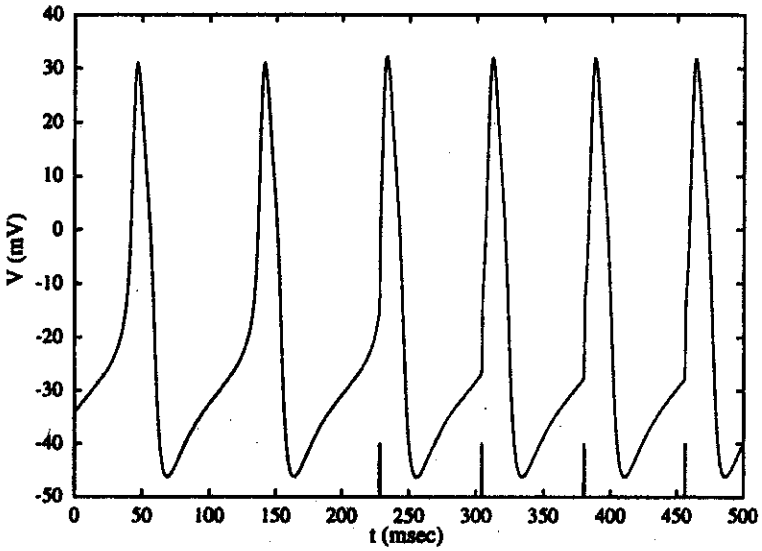

Figure 7.13
Phase-locking (1:1) of the Morris-Lecar model to a series of four current pulses with interpulse period of 76 msec. Intrinsic period of the membrane oscillator is 95 msec. Parameters are as in figure 7.12B. After phase-locking is achieved, the stimulus is seen to occur about 67 msec after the action potential's peak, just as predicted by the PRC.

method of averaging, used successfully to study the dynamics of two or more neural oscillators that are *weakly coupled* (e.g., Hansel, Mato, and Meunier 1995; Ermentrout and Kopell 1991). In this limit, the coupling is sufficiently weak that each oscillator's trajectory remains close to its intrinsic limit cycle. The primary effect of the coupling is to perturb the relative phase between the oscillators, much as we described above. Because the perturbation per cycle is small (with weak coupling), however, the net effect occurs only over many cycles, and the per cycle effect is seen as averaged. For illustration, we summarize the use of averaging to describe the phase-locking properties of two identical Morris-Lecar oscillators when coupled with identical mutually excitatory synapses. Detailed derivations of the equations can be found in the above-mentioned papers.

We assume that motion of each oscillator along its limit cycle can be rewritten in terms of a phase variable. Thus an oscillator's membrane potential is periodic with period T and follows the function $V(\theta_j)$, where θ_j is the phase of the jth oscillator, $j = 1, 2$, and V is the voltage component of the limit cycle trajectory. In the absence of coupling, the dynamics are given simply as $\theta_j = t + C_j$, where C_j is an arbitrary

phase shift. Now consider the effect of small coupling. A brief, weak synaptic current I_{syn} to cell i from activity in cell j will cause a phase shift in cell i:

$$\Delta\theta_i = -V^*(\theta_i(t))I_{syn}(\theta_i(t), \theta_j(t)), \tag{7.27}$$

where $V^*(t)$ is the infinitesimal phase response function, the minus sign converts excitatory current to positive phase shift. The synaptic current is given by

$$I_{syn}(\theta_i, \theta_j) = g_c\alpha(\theta_j(t))(V(\theta_i(t)) - V_{syn}), \tag{7.28}$$

where the postsynaptic gating variable $\alpha(t)$ is cell i is activated by the presynaptic voltage $V(\theta_j)$, V_{syn} is the reversal potential for the synapse, and g_c is the strength of the synaptic coupling. The gating variable $\alpha(t)$ could be represented by a so-called (event-triggered) alpha function introduced by Rall (cf. chapter 2, this volume). Alternatively, it could obey a voltage-gated differential equation.

In the method of averaging we simply "add up" all the phase shifts due to the synaptic perturbations and average them over one cycle of the oscillation. Thus, after averaging, the coupled system is found to satisfy

$$\frac{d\theta_1}{dt} = 1 + g_cH(\theta_2 - \theta_1) + O(g_c^2) \tag{7.29}$$

$$\frac{d\theta_2}{dt} = 1 + g_cH(\theta_1 - \theta_2) + O(g_c^2), \tag{7.30}$$

where H is a T-periodic "averaged" interaction function, given by

$$H(\phi) = \frac{1}{T}\int_0^T V^*(t)\alpha(t+\phi)(V_{syn} - V(t))\,dt. \tag{7.31}$$

The key to these models is the computation of H (see Ermentrout and Kopell 1991; Kopell 1988).

In figure 7.14A, we show the function $V^*(t)$ along with the synaptic gating variable $\alpha(t)$ over one cycle for exactly the same parameters as in figure 7.12B. Here $\alpha(t) = 0.04\,te^{-t/5}$ is an alpha-function with a 5 msec time constant. Note the similarity (except for scale) of the excitatory PRC and the infinitesimal PRC, $V^*(t)$. As with the PRC, $V^*(t)$ is mainly positive, showing that the predominant effect of depolarizing perturbations is to advance the phase or, equivalently, to speed up the oscillator. In only a very small interval of time can the phase be delayed, and this is a general property of membranes that become oscillatory through a saddle node bifurcation (Ermentrout 1996).

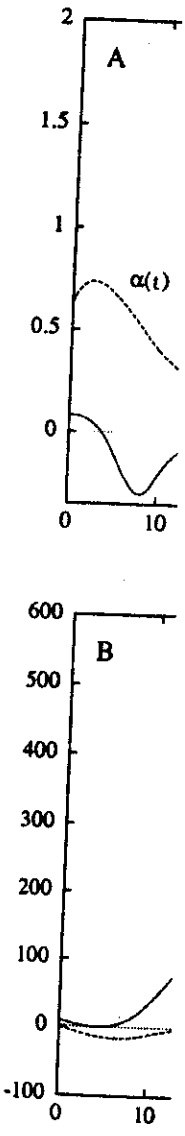

Figure 7.14
The method of av
oscillators are as i
line shows the infi
aptic conductance
5 msec time consta
20 mV. (B) Interac
and a synaptic reve
to the weakly coup

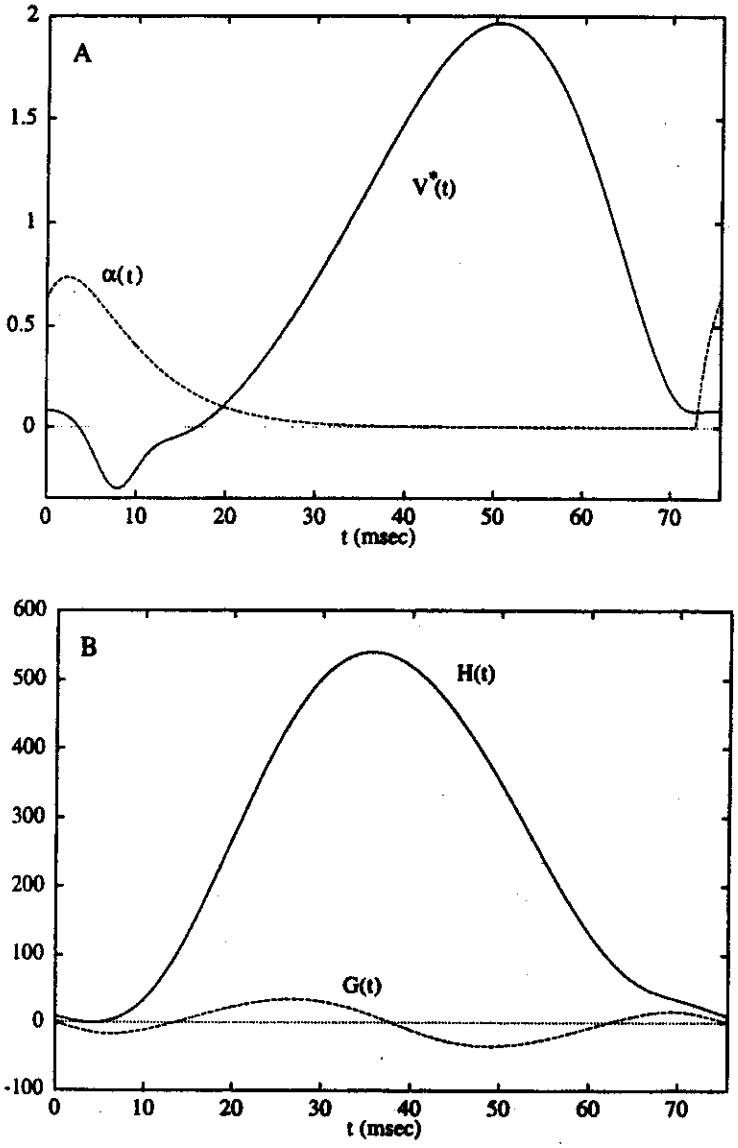

Figure 7.14
The method of averaging for two weakly coupled identical Morris-Lecar oscillators. Parameters for the oscillators are as in figures 7.4–7.6 (and figure 7.12A) and an applied current $I = 50\,\mu A/cm^2$. (A) Solid line shows the infinitesimal PRC, $V^*(t)$ and the dashed line shows the time course of the excitatory synaptic conductance (for plotting convenience, here multiplied by ten), modeled as an alpha function with a 5 msec time constant and peak of about $0.075\,mS/cm^2$. The alpha function "turns on" when V crosses 20 mV. (B) Interaction function $H(t)$ and its odd part $G(t)$ for the synaptic dynamics shown in panel A and a synaptic reversal potential of 0 mV. Zeros of the function $G(t)$ correspond to phase-locked solutions to the weakly coupled system; stable solutions have positive slopes and unstable have negative slopes.

Figure 7.14B shows the function $H(t)$ defined in eq. 7.31 for that figure's alpha function and for $V_{syn} = 0\,\text{mV}$. We can use this function along with eqs. 7.29–7.30 to determine the stable phase-locked patterns for this coupled system. Let $\Theta = \theta_2 - \theta_1$ denote the phase difference between the two oscillators. From eqs. 7.29–7.30 we see that Θ satisfies

$$\frac{d\Theta}{dt} = g_c(H(-\Theta) - H(\Theta)) + O(g_c^2) \equiv -2g_c G(\Theta) + O(g_c^2). \tag{7.32}$$

Here $G(\Theta)$ is just the odd part of the function H. Because the coupling is weak, the higher-order terms, $O(g_c^2)$ are ignored. Equation 7.32 is just a first-order equation. Phase-locked states are those for which Θ does not change, that is, they are roots of the function $G(\Theta)$ and they are stable fixed points if $G'(\Theta) > 0$. Because any odd periodic function has at least two zeros, $\Theta = 0$ and $\Theta = T/2$, there will always exist phase-locked states, although, these may not be stable. Synchronous solutions ($\Theta = 0$) imply that both membranes fire together. Antiphase solutions ($\Theta = T/2$) are exactly one-half cycle apart. Figure 7.14B shows the function $G(\Theta)$, from which we see there are four distinct fixed points: the *synchronous* (precisely in-phase) solution; the *antiphase* solution; and a pair of phase-shifted solutions at $\Theta \approx \pm 15\,\text{msec}$. Both the synchronous and antiphase solutions are unstable but the phase-shifted solution is stable. Thus, if two of these oscillators are coupled with weak excitatory coupling and the parameters chosen as above, they will phase-lock with a phase shift of about 20% of the period. Although the classical view is that mutual excitation leads to perfect synchrony, computations with a variety of neuronal models suggest that this is not generally the case.

This type of analysis is easily extended to systems where the oscillators are not exactly identical, coupling is not symmetric, and there are many more oscillators. The behavior of such phase models and the forms of the interaction functions, H, are the topics of current research.

7.6 Summary

We have introduced and used some of the basic concepts of the qualititative theory of differential equations to describe the dynamic repertoire of a representative model of excitability. We believe that a geometrical treatment, as in the phase plane, gives one an opportunity to see more clearly and to appreciate the underlying qualitative structure of models. One can see which initial conditions, for example, those resulting from a brief perturbing stimulus, will lie in the domain of attraction of any particular stable steady state or limit cycle. This is especially helpful for the design of experi-

ments to switch a multistable system from one mode to another. Analytic methods are also important—for determining and interpreting the stability of solutions (e.g., eq. 7.19 for the Hopf bifurcation) and for approximating aspects of the solution behavior (e.g., eq. 7.25 for phase-locking). Another useful conceptual device is the bifurcation diagram by which we have provided compact descriptions of the system attractors. Although in several of our illustrations, the bifurcation parameter was I, and the steady-state I-V relation appeared explicitly in the diagram, channel density, synaptic weight (as in the Wilson-Cowan network model), or any other parameter can be used.

We have shown how a minimal but biophsically reasonable membrane model can be massaged to exhibit robustly a variety of physiologically identifiable firing behaviors. For the simplest two-variable Morris-Lecar model, we illustrated some qualitative differences in threshold behavior. When the steady-state current-voltage relation is monotonic, action potential size may be graded, although generally quite steeply with stimulus strength, and latency for firing is finite; when it is N-shaped, there is a true (saddle point) threshold for action potentials, latency may be arbitrarily long, and intermediate-sized responses are not possible. Correspondingly, for a steady stimulus, the monotonic case leads to onset of oscillations with a well-defined, nonzero frequency (Hopf bifurcation), and with possibly small amplitude (supercritical). In contrast, in the N-shaped case repetitive firing first appears with zero frequency (homoclinic bifurcation). These features are consistent with some of those used by Hodgkin (1948) to distinguish axons with different repetitive firing properties, class II and class I, respectively. Additionally, we have provided a geometric interpretation of some common forms of bursting neurons. Many bursters can be dissected into fast dynamics coupled to one or more slow processes that move the fast dynamics between resting and oscillatory states. Coupled and forced oscillators can often be reduced to maps or to continuous low-dimensional systems of phase equations, especially when the interactions are weak.

With regard to implementation of models, there are sophisticated software packages and subroutines available nowadays to help make theoretical experimentation and analysis a real-time endeavor; the "tooling-up" time is greatly reduced. Programs like XPP incorporate a mix of numerical integration and analytic formulation (linear stability analysis, bifurcation analysis, averaging—carried out numerically) with graphical representation all in an interactive framework. (The numerical methods employed by XPP are described in chapter appendix B.) To set up and get the Morris-Lecar model running should take less than fifteen minutes. Although we have used XPP here for the two-variable model, it can also deal with higher-order systems (like the bursting models of section 7.4). Stability of steady states can be computed,

and time courses plotted interactively. The generalization of nullclines to surfaces is not available computationally, but two-variable projections of trajectories from the higher-order phase space can be insightful (e.g., figure 7.9). A widely distributed subroutine we have also found valuable for dissecting nonlinear systems in AUTO (Doedel 1981), which automatically generates bifurcation diagrams (as in figures 7.2, 7.6, 7.7; see chapter appendix B). The main components of AUTO are included in the package XPP, thus making AUTO an interactive program. We used XPP-AUTO for the fast/slow analysis of the bursting models in section 7.4. For the evaluation and algebraic manipulation of analytic prescriptions (e.g., lengthy perturbation and bifurcation formulas), many modelers have used symbol manipulation programs like Mathematica and MAPLE with success (see Rand and Armbruster 1987). As regards numerical packages, we advise that one be generally familiar with the methods being employed, and with their limitations. It is not so uncommon to pose a problem that seems to just miss the criteria for suitablity of a given technique—and one should be careful to recognize the symptoms of breakdown of the particular method being used.

Finally, we emphasize the value of using idealized, but biophysically reasonable, models in order to capture the essence of system behavior. If models are more detailed than necessary, identification of critical elements is often obscured by too many possibilities. On the other hand, if justified by adequate biophysical data, more detailed models are valuable for quantitative comparison with experiments. The modeler should be mindful and appreciative of these two different approaches: which one is chosen depends on the types of questions being asked and how much is known about the underlying physiology.

Acknowledgment

Bard Ermentrout was partially supported by National Science Foundation grant DMS 96–728. Much of John Rinzel's contribution to this chapter was completed while he was with the Mathematical Research Branch, NIDDK at the National Institutes of Health.

Appendix A: Morris-Lecar Equations

The differential equations and V-dependent functions are

$$C\frac{dV}{dt} = -\bar{g}_{Ca}m_\infty(V)(V - V_{Ca}) - \bar{g}_K w(V - V_K) - \bar{g}_L(V - V_L) + I \tag{7.33}$$

$$\frac{dw}{dt} = \phi\frac{[w_\infty(V) - w]}{\tau_w(V)}, \tag{7.34}$$

where

$$m_\infty(V) = 0.5 * [1 + \tanh\{(V - V_1)/V_2\}], \tag{7.35}$$

$$w_\infty(V) = 0.5 * [1 + \tanh\{(V - V_3)/V_4\}], \tag{7.36}$$

and

$$\tau_w(V) = 1/\cosh\{(V - V_3)/(2 * V_4)\}. \tag{7.37}$$

For Figures 7.1–7.3, we use the parameters $V_1 = -1.2$, $V_2 = 18$, $V_3 = 2$, $V_4 = 30$, $\bar{g}_{Ca} = 4.4$, $\bar{g}_K = 8.0$, $\bar{g}_L = 2$, $V_K = -84$, $V_L = -60$, $V_{Ca} = 120$, $C = 20\,\mu\text{F/cm}^2$, and $\phi = 0.04$. (All conductances are in mS/cm^2 and voltages in mV.) These same parameters are used for figures 7.4–7.6, with the following exceptions: $V_3 = 12$, $V_4 = 17.4$, $\bar{g}_{Ca} = 4.0$, and $\phi = 1/15$. In figures 7.7–7.8, the parameters are as in figures 7.4–7.6 but $\phi = 0.23$. The current, I (in $\mu\text{A/cm}^2$), is generally the only free parameter.

Appendix B: Numerical Methods

Most of the figures shown in this chapter were produced by numerically solving the Morris-Lecar equations. We have used a program XPP, written by Bard Ermentrout, which uses a variety of numerical integration methods to solve the equations on any computer that runs X-windows. It is available via anonymous ftp from ftp.math.pitt.edu/pub/bardware, and there is an extensive tutorial geared toward neurobiology available on the World Wide Web at http://www.pitt.edu/~phase. For the all but the bursting simulations, we have used a fourth-order Runge-Kutta algorithm. The bursting simulations employed a variable-time-step Gear algorithm (Press et al. 1986).

For the Morris-Lecar model, the nullclines can be found explicitly by solving each of the equations for w as a function of v, although this is generally not easy and thus calls for numerical techniques. All of the phase plane pictures were found by numerically computing the nullclines. This is done by breaking the phase plane into many small boxes, evaluating the functions on each point, and then using a linear interpolation to find the zero contours.

Singular points are found using Newton's method with a numerically computed Jacobian. Once a steady state is found, the Jacobian is computed and the QR algorithm is used to find the eigenvalues. These determine the stability of the singular point.

For certain steady states in the Morris-Lecar model, we want to find special trajectories called the "unstable" and "stable manifolds." This is done by computing an eigenvector for a particular eigenvalue (the eigenvectors are tangent to these manifolds) by inverse iteration. Once the eigenvector is known, the equations are integrated either forward or backward in time with initial conditions that are on the eigenvector and slightly off of the singular point.

The qualitative behavior of higher-dimensional systems as a parameter is varied can be understood and described compactly by determining the bifurcation diagrams. AUTO (Doedel 1981) was used in this chapter (through its interface with XPP) to trace, essentially automatically, the bifurcation curves as any parameter is varied. This program is able to find all steady states and periodic solutions regardless of their stability. The characteristics of stability, eigenvalues for steady states and Floquet exponents for periodic solutions, are computed along with the frequencies of periodic solutions. Two-parameter bifurcation diagrams (similar to figure 7.11C) indicating where steady states and periodic solutions exist and where they gain or lose stability can also be computed by AUTO.

The computation of the "infinitesimal PRC" is done automatically as part of the XPP package. Essentially, it solves an allied linear equation until a particular periodic orbit is found. The integral required for averaging is automatically computed.

A general and practical reference to many of the above numerical methods, which also leads to more literature, is Press et al. 1986.